Analysis of Temperature Dependence of Nitride-based Quantum Cascade Detectors

by

A. F. M. Saniul Haq

Student ID: 0412062205

A thesis submitted in partial fulfillment

for the degree of **Master of Science**

in the

Department of Electrical and Electronic Engineering

Bangladesh University of Engineering and Technology

July, 2014

Declaration

It is hereby declared that this thesis or any part of it has not been submitted elsewhere for the award of any degree or diploma.

(**A. F. M. Saniul Haq**)

Approval Certificate

The thesis titled "Analysis of Temperature Dependence of Nitride-based Quantum Cascade Detectors" submitted by A. F. M. Saniul Haq, Student ID: 0412062205, Session: April 2012 has been accepted as satisfactory in partial fulfillment of the requirement for the degree of MASTER OF SCIENCE IN ELECTRICAL AND ELECTRONIC ENGINEERING on 19 July, 2014.

Board of Examiners

1.__________________________________ Chairman (Supervisor)

Dr. Muhammad Anisuzzaman Talukder
Associate Professor,
Department of EEE, BUET,
Dhaka-1205, Bangladesh

2.__________________________________ Member (Ex-Officio)

Dr. Taifur Ahmed Chowdhury
Professor and Head,
Department of EEE, BUET,
Dhaka-1205, Bangladesh

3.__________________________________ Member

Dr. Md. Ziaur Rahman Khan
Professor,
Department of EEE, BUET,
Dhaka-1205, Bangladesh

4.__________________________________ Member (External)

Dr. Mohammad Mojammel Al Hakim
Associate Professor,
Department of EEE,
East West University

Abstract

QCDs are emerging technology which has shown to encompass wavelengths from near-infrared to the THz region. The design of QCDs has proven to be robust and reliable. Especially in the MIR range around 4 to 16 μm, well-established semiconductor material systems and processing procedures are available. MIR range also holds signature absorption peaks for some greenhouse gases that has significant environmental and chemical application. Again nitride based material system demonstrate superior performance in terms of large LO-phonon energy, current capacity, electron mobility, break-down voltage, and efficiency for power module and photovoltaic applications. In this thesis, a nitride based material system simulator is developed using the inherent strain and polarization effect of the nitride material. The simulator solves the band structure and energy values of a nitride based quantum cascade structure. Moreover two designs of nitride based QCD operating in the mid-infrared region are presented along with a detail transport and performance analysis. This thesis also attempts to study important parameters of the nitride based detectors as function of detector temperature. The strongly varying device resistance and the drop in responsivity with temperature of the mid-infrared quantum cascade detectors are numerically calculated based on a model describing LO-phonon assisted transitions between the different involved states of the quantum cascade.

Acknowledgements

I would first like to thank Almighty Allah for His continuous blessings upon me, especially where my education is concerned. These two years of my M. Sc. Engineering course, though stressful sometimes, could not be easier if I would not have the mental strength provided by Him to cope with.

Next, I would like to express my never-ending gratitude towards my thesis supervisor, **Dr. Muhammad Anisuzzaman Talukder**. From the very beginning of my thesis work and throughout the whole period, his continuous guidance made it possible to accomplish my goal. The systematic way in which this thesis has been written is solely due to his insight and analytical prowess. I also learnt many important and efficient ways and tactics for research from him. I shall be ever indebted to him for teaching me various aspects of quality writing. His knowledge and research power have always encouraged me to try my best to do something substantial.

This thesis work would never end without the constant helps from my fellow researchers, Golam Md. Imran Hossain, Asif Ahmed, Orchi Hassan, Md. Shahadat Hasan Sohel, and Fariah Hayee. I could not ask for a more helpful and more friendly research partners. I am also thankful to **HEQEP CP-2091** project for the funding to carry out this work.

I would like to dedicate this work to my parents, who had always been the mentors of my life. I thank them wholeheartedly for the belief they have in me and their support towards my judgement regarding my studies.

Finally, We would like to thank all our friends and classmates for making our BUET life as memorable as it has been. Life in BUET has been a pleasant one only because of them.

Contents

Declaration **i**

Approval Certificate **ii**

Abstract **iii**

Acknowledgements **iv**

Table of Contents **vi**

List of Figures **ix**

List of Tables **xiii**

1 Introduction **1**

1.1 Historical Overview of Intersubband Transition 2

1.2 Group-III Nitrides 4

1.3 Group III- Nitrides for Infrared Optoelectronics: Motivations 6

1.4 Organization of the Thesis 9

2 Group III Nitrides **11**

2.1 Introduction 11
2.2 Material Properties 11
2.3 Crystalline Structure 12
2.4 Electrical and Optical Parameters 14
2.5 Polarization and Electric Field 17
2.6 Results and Discussion 22
2.6.1 AlN/GaN Superlattice 22
2.6.2 Quantum Cascade Detector (QCD) 24
2.6.3 Quantum Cascade Laser (QCL) 25
2.7 Summary 27

3 Theoretical Framework **29**

3.1 Introduction 29
3.2 Intersubband Transitions in Quantum Wells 29
3.3 Absorption Coefficient of a Single Quantum Well 32
3.4 Detector Physics 34
3.4.1 Zero Bias Resistance (R_0A) 34
3.4.2 Absorption 37
3.4.3 Quantum Efficiency 38
3.4.4 Responsivity 39
3.4.5 Detectivity 40
3.5 Summary 40

4 Results and Discussion **42**

4.1 Introduction 42
4.2 Verification of Developed Simulator 42

4.2.1 GaAs/AlGaAs QCD 43
4.2.2 InGaAs/InAlAs QCD 45
4.2.3 GaN/AlGaN QCD 49
4.3 Proposed Mid-Infrared GaN/AlN QCD 52
4.3.1 Nitride QCD Design-1 53
4.3.1.1 Device Structure 53
4.3.1.2 Transport Mechanism of the Device 54
4.3.1.3 Zero Bias Resistance 56
4.3.1.4 Current Density 58
4.3.1.5 Absorption Coefficient Variation over Temperature 58
4.3.1.6 Quantum Efficiency 60
4.3.1.7 Responsivity Variation over Temperature . 61
4.3.2 Nitride QCD Design-2 62
4.3.2.1 Device Structure 62
4.3.2.2 Transport Mechanism of the Device 63
4.3.2.3 Zero Bias Resistance 64
4.3.2.4 Current Density 66
4.3.2.5 Absorption Coefficient Variation over Temperature 67
4.3.2.6 Quantum Efficiency 67
4.3.2.7 Responsivity Variation over Temperature . 68
4.4 Summary 70

5 Conclusion **72**

List of Figures

1.1 Spectral coverage by interband and ISB devices based on different material systems [1]. 7

2.1 Bandgap versus lattice constant for group III nitrides. . . . 13

2.2 Left: hexagonal structure of wurtzite GaN with A, B bilayers. Right: wurtzite GaN unit cell. Ga-atoms are red (dark), N-atoms are blue (bright). c_0 and a_0 are the lattice constants, u_0 is the anion-cation bond length. 13

2.3 Left: Ga-face crystal in the [0001] direction. Right: N-face crystal in the [0001] direction. Ga-atoms are red (dark), N-atoms are blue (bright). 14

2.4 Sketch of a pseudomorphically grown layer under compressive strain (top panel) and tensile strain (bottom panel). . . 21

2.5 QCL Simulation results of 15 Å AlN/GaN superlattice. . . . 23

2.6 QCL Simulation results of 30 Å AlN/GaN superlattice. . . . 23

2.7 QCL Simulation Package results of AlN/GaN superlattice QCD. 24

2.8 QCL Simulation Package results of AlN/GaN superlattice QCD designed to operate at 1.7 μm. 26
2.9 QCL Simulation results of conduction band profile of c-plane design of a THZ QCL. 27
2.10 QCL Simulation Package results of conduction band profile of a-plane design of a THZ QCL. 28

4.1 Band structure of GaAs/AlGaAs QCD operating at 9μm. . . 44
4.2 R_0A of GaAs/AlGaAs QCD operating at 9μm [2]. 44
4.3 Absorption coefficient of GaAs/AlGaAs QCD designed to operate at 9μm. 45
4.4 Responsivity of GaAs/AlGaAs QCD designed to operate at 9μm. 46
4.5 Band structure of InGaAs/InAlAs QCD operating at 9μm. . 47
4.6 R_0A of InGaAs/InAlAs QCD operating at 9μm [3]. 47
4.7 Absorption coefficient of InGaAs/InAlAs QCD operating at 9μm. 48
4.8 Responsivity of InGaAs/InAlAs QCD operating at 9 μm. . . 49
4.9 Band structure of GaN/AlGaN QCD designed to operate at 1.85 μm. 50
4.10 R_0A of GaN/AlGaN QCD designed to operate at 1.85 μm [4]. 50
4.11 Absorption coefficient of GaN/AlGaN QCD operating at 1.85 μm. 51
4.12 Responsivity of GaN/AlGaN QCD operating at 1.85 μm. . . 52

4.13 Band structure and the relevant moduli squared wavefunctions for active/relaxation region of design-1 at 200 K temperature. The layer sequence of a period of the structure, is 40/ **20**/ 15/ **22**/ 19/ **25**/ 26/ **23**, where the layer sequences are given in Å, $Al_{0.3}Ga_{0.7}N$ barriers are in bold face, GaN wells are in normal face, and numbers underlined correspond to the n-doped layers (5×10^{17} cm^{-3}). 54
4.14 Schematic representation of QCD energy levels. 55
4.15 Carrier Density variation over temperature for designed GaN/AlN QCD design-1. 57
4.16 Current Density variation over temperature for designed GaN/AlN QCD design-1. 58
4.17 Absorption coefficient variation over temperature for designed GaN/AlN QCD design-1. 59
4.18 Escape probability variation over temperature for designed GaN/AlN QCD design-1. 60
4.19 Responsivity variation over temperature for designed GaN/AlN QCD design-1. 61
4.20 Peak Responsivity variation over temperature for designed GaN/AlN QCD design-1. 62

4.21 Band structure and the relevant moduli squared wavefunctions for active/relaxation region of design-2 at 200 K temperature. The layer sequence of a period of the structure, is 30/ **23**/ 14/ **23**/ 18/ **28**/ 28/ **26**, where the layer sequences are given in Å, $Al_{0.3}Ga_{0.7}N$ barriers are in bold face, GaN wells are in normal face, and numbers underlined correspond to the n-doped layers (5×10^{17} cm^{-3}). 63
4.22 Carrier Density variation over temperature for designed GaN/AlN QCD design-2. 65
4.23 Zero bias resistance and current density for designed GaN/AlN QCD design-2 for T = 50 K to T = 300 K. 65
4.24 Zero bias resistance variation for different nitride based QCD for T = 77 K and T = 200 K. 66
4.25 Absorption coefficient variation over temperature for designed GaN/AlN QCD design-2. 67
4.26 Escape probability variation over temperature for designed GaN/AlN QCD design-2. 68
4.27 Responsivity variation over temperature for designed GaN/AlN QCD design-2. 69
4.28 Peak Responsivity variation over temperature for designed GaN/AlN QCD design-2. 69

List of Tables

2.1 Electro-optical material parameters 17

2.2 Polarization calculating parameters 19

2.3 Elastic constants for Strain 20

2.4 Energy values between different energy levels 23

4.1 Values of some transition rates in Nitride QCD design-1 . . . 56

4.2 Values of some transition rates in Nitride QCD design-2 . . . 64

Chapter 1

Introduction

Optical intersubband transitions in quantum wells were first observed in 1985 by two researchers at Stanford University, West and Eglash [5]. Owing to the theoretical description which involved the envelope function approximation, they called this novel optical phenomenon a "quantum well envelope state transition (QWEST)". These transitions take place between electronic states located entirely in the conduction band. The quantum wells of West and Eglash consisted of thin GaAs layers sandwiched between AlGaAs barriers. In their pioneering work, they pointed out the possibility of tuning the narrow QWEST resonance by varying the well width; and they also immediately proposed its usage for fast optical digital logic devices.

1.1 Historical Overview of Intersubband Transition

This discovery by West and Eglash opened the era of intersubband transitions for optical and optoelectronics applications which culminated in 1994 with the realisation of quantum cascade lasers at AT&T Bell laboratories by Faist et al. [6].

On the detection side, intersubband transitions were extensively investigated by Levine et al. at AT&T Bell laboratories, as well as by Harwit and Harris at Stanford University, who characterised both the strong absorption and the Stark shift of such intersubband transitions in AlAs/GaAs supperlattices [7, 8]. This resulted in the implementation of the first 10 μm quantum well infrared photodetector (QWIP) by Levine et al. in 1987 [9]. Since then, many other people have made important contributions to the understanding, physical mechanism, and performance of QWIPs; a substantial amount of this progress has been published by Levine in an excellent review article [10] and by Liu in a comprehensive book chapter [11].

In the context of this thesis, the work of Schneider at Fraunhofer-Institut f*ü*r Angewandte Festk*ö*rper physik is of special interest [12]. In 1993, he was the first to propose the use of asymmetrical quantum well structures, effectively producing an internal electric field. Such a device can be operated in photovoltaic mode, i. e., without external bias. Schneider et al. showed theoretically that this should lead to an optimized performance

for operation under high photon fluxes or long integration times in the long wavelength range (8 μm – 12 μm) [12]. Schneider et al. reported also the successful operation of a photovoltaic QWIP in the GaAs/AlGaAs material system at 77 K with maximum peak detectivity of 5.1×10^9 Jones [13]. In this device, the asymmetry was achieved by insertion of an additional, energetically higher, and very thin barrier layer on one side of the well. Later on, Schneider et al. performed high-speed characterization of the same device at room temperature, which led to measured rise and decay times of 12 ps and 65 ps, respectively [14].

QWIPs have also been realised in other material systems. Hasnain et al. demonstrated successful detection at 3 μm – 5 μm with structures grown in lattice matched InGaAs/InAlAs on InP [15], where the higher conduction band offset of this material system allowed to go for shorter wavelengths. The accessable wavelength range has also be extended to the "very long wavelength" range 14 μm – 20 μm by Sarusi et al. in 1994 [16]. In 2004, Gendron et al. at Thales Research and Technology, France published their work on quantum cascade detector (QCD) [17] using the GaAs material system, where the term *quantum cascade detector* was first coined. Apparently, the term has already been defined in a french patent application by Berger in 2001 [18]. QCDs have been introduced as the alternative photovoltaic version of QWIPs which are designed with multiple periods cascaded for successive electronic relaxations in the cascade.

1.2 Group-III Nitrides

The III-nitride semiconductors are the important and auspicious materials for optoelectronic and electronic applications. Being direct wide bandgap semiconductors, III-nitrides are the choice for light-emitting diodes (LED) to cover spectral range from deep UV (high Al content AlGaN/GaN system) to green (InGaN/GaN system) using quantum wells (QWs) as an active medium. Group III-nitride LEDs have already found a number of applications, including indoor and outdoor illumination, traffic and emergency vehicle signals, data storage, water purification, disinfection of medical tools and etc. LED technology, prompted by spectacular progress in terms of efficiency, output power and spectral coverage in the last two decades, is a rapidly progressing field of research.

GaN technologies are also very promising for high-power applications in the microelectronics field. III-nitrides have superior material properties, such as higher electrical breakdown field (from 3.3 MV/cm for GaN to 11.7 MV/cm for AlN), high electron mobility (2000 cm^2/V-s), and wide bandgap (from 3.4 eV for GaN to 6.2 eV for AlN) in comparison with Si or GaAs material systems conventionally used for electronic components. GaN-based devices demonstrate superior performance in terms of breakdown voltage, current capacity, high frequency, efficiency, and reduced size of the power modules.

Another prospect field for III-nitride materials is photovoltaics. The inter-

est to III-nitrides for solar applications stems from the possibility to make InGaN alloys optically active over the full spectrum of sunlight. This is an alternative to multi-junction cells approach with potential efficiency up to 60% (compared to the theoretical limit of 30% for silicon technology). However, due to immature epitaxial growth methods for In-rich alloys and insufficient knowledge of material properties, only preliminary prototypes for InGaN solar cells have been reported, leaving a space for future research activities [19, 20].

However, the GaN technology has several drawbacks associated to the defect structure of epitaxial films and the lack of cheap substrates for homoepitaxial growth. In order to make III-nitrides an economically-competitive technology, silicon wafers are pursued as an alternative substrate choice. However, GaN and AlGaN layers are highly strained when epitaxially deposited on Si substrates with <111> crystal orientation and a large difference in thermal coefficients between GaN and Si leads to decohesion and cracking. However, recent progress on in situ growth monitoring methods has made it possible to produce GaN on 8 inch silicon wafers using metal organic chemical vapor deposition (MOCVD) [1].

1.3 Group III- Nitrides for Infrared Optoelectronics: Motivations

As described above, GaN-based semiconductors have rapidly become the materials of choice for UV-blue-green optoelectronics. Much less effort has been devoted to InN and In-rich alloys, which appeared as the natural nitride-based choice for red optoelectronics. A major breakthrough in 2002, stemming from much improved quality of InN films grown using molecular beam epitaxy (MBE), resulted in the bandgap of InN being revised from 1.9 eV to a much narrower value of 0.64 eV (1.9 μm wavelength) [21]. This finding extended the interband optoelectronic capabilities of the III-nitride family into the infrared (IR) spectral region. However, this IR technology is penalized by the high residual doping, poor thermal stability and surface effects characteristic of InN [19].

Thus, an alternative approach, using intersubband (ISB) transitions, has been proposed to develop an IR technology. The IR spectral region is well covered with optical devices based on the III-As and III-P material systems as shown in Fig. 1.1. ISB devices, mainly detectors and lasers for applications in gas sensing, medicine and chemical industry using GaInAsN/AlAs [22], GaAs/AlGaAs [23, 24], and GaInAs/AlAsSb [25, 26] have been well developed and can be tuned from mid- to far-IR regions. However, this technology cannot be easily extended to the near-IR due to the small conduction band offset of these materials, neither can it cover the range from 30 to 40 μm [27], which corresponds to the Reststrahlen band

in arsenides. With the large conduction band offset of 2.0 eV between GaN and AlN and the progress achieved in epitaxial growth of thin III-N films, the gaps in As technologies are now accessible using III-nitride materials. In contrast to InAs/AlSb materials, the lateral valleys of GaN and AlN are placed high in energy, which opens prospects for near-IR intersubband light emitters.

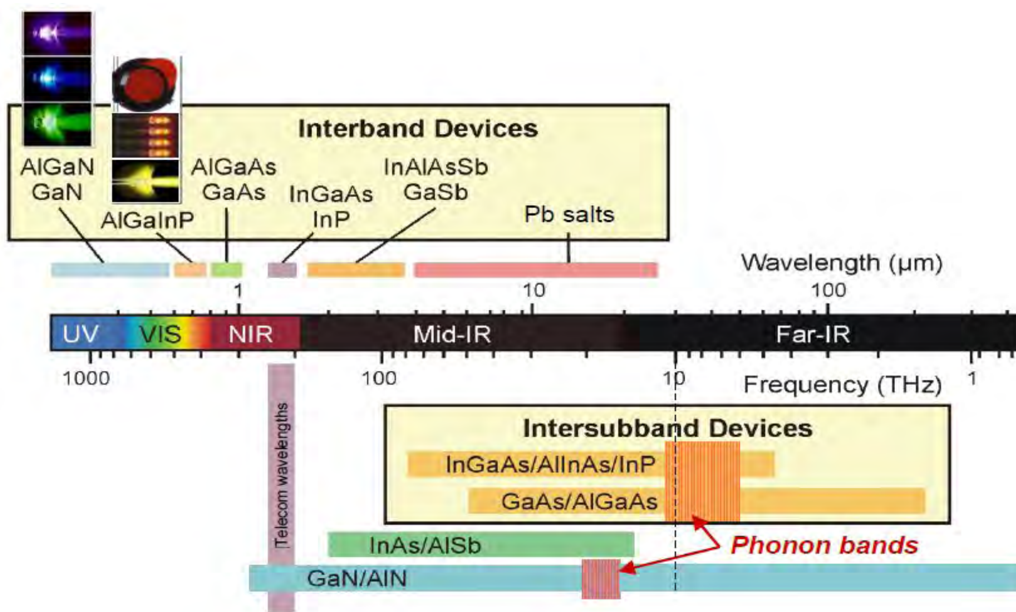

Figure 1.1: Spectral coverage by interband and ISB devices based on different material systems [1].

Rapid progress has been made in terms of device performance. To date, THz QCLs have been demonstrated in the 0.85 – 5 THz range [28], with pulsed operation up to 186 K [29], and output powers of up to 250 mW pulsed [30]. However, GaAs-based QCLs have limitations of thermal back-filling and thermally activated phonon scattering which make it impossible

for operation of the device at room temperature. These drawbacks can be overcome using III-N material systems, thanks to the large LO-phonon energy of 92 meV of GaN, which significantly exceeds the room-temperature thermal energy. Additionally, strong electron-phonon interaction provides possibility to perform ultrafast devices with rapid depopulation of the lower laser state [31].

The aim of this work is to improve the performance and the understanding of the material issues involved in the GaN/AlGaN ISB technology. As optical and electrical performance of the ISB devices depends on the quality of the epilayers, it is important to study the issues like strain management in the device active region, i.e. in GaN/AlGaN superlattices (SLs). Furthermore, targeting longer wavelength, i. e., smaller energy separation between energy levels, implies enhanced doping of the heterostructures in order to observe ISB absorption. Therefore, considerable attention has to be devoted to silicon doping and the associated many-body effects. With this knowledge, this work concentrates on the design and analysis of ISB detectors for mid-IR spectral region based on the quantum cascade principle.

This work was funded by HEQEP sub-project (CP-2091), initiated on June 2012, which aimed at the assessment of the mid-infrared technology for the development of a new generation of high-performance IR optoelectronic devices.

In this work, the Schrödinger equation has been solved to calculate the electronic band structures of intersubband heterostructures. The simulation tool was developed using Matlab. Since the nitride material system is not well defined yet, the development of the nitride library was quite challenging. A simulation tool was also developed to study the electronic transport of the device using the scattering rates in between the states with Fermi's Golden Rule. The calculated scattering rates have been used to calculate the zero-bias resistance, absorption coefficient, quantum efficiency and responsivity of the detectors. Based on the temperature dependent performance of the detectors, an optimized QCD has been designed and detail analysis has been presented.

1.4 Organization of the Thesis

This thesis is a contribution to the study of nitride based QCD designed to exhibit ISB absorption in the mid-IR spectral region. It starts with this introductory chapter 1, which gives a short historical overview of intersubband transitions and the advantages and challenges associated to the wurtzite III-nitride material system. Particularly, chapter 1 present the key application fields for III-N semiconductors and justify the motivation of this work.

Chapter 2 introduces the properties of the nitride material which lies the base of this work. The crystalline structure with its inherent polarity feature, electronic properties, and internal electric fields in wurtzite III-N

semiconductors are discussed. This chapter also describes the verification of the developed simulator for nitride based material system by comparing with different reported nitride based structure including a superlattice structure, a tera-hertz QCL, and a QCD.

The theoretical model developed for simulation of quantum cascade structures are described in chapter 3. Schrödinder's equation and Fermi's golden rule, which are used in the calculation of wavefunction and absorption in quantum wells, is described in this chapter. Different performance parameters such as the zero bias resistance, absorption coefficient, quantum efficiency, and responsivity of the detectors are also presented in this chapter.

Chapter 4 focuses on the performance characterization of nitride based QCDs. In the beginning of the chapter, studies of different QCDs of different material system in the wavelength range from 1 μm to 9 μm are presented. Then two designs of nitride based QCD operating in the mid-infrared region are presented along with a detail transport and performance analysis.

Chapter 2

Group III Nitrides

2.1 Introduction

GaN is the most studied group III nitride compound, but compared to GaAs, there is still relatively little known about GaN. Even for GaN material parameters, values reported in the literature can vary depending on the growth method and material quality. As for InN, a less mature group III nitride compound, researchers only recently agreed to a bandgap value of 0.7 eV [32]. The focus of this work is on QCDs based on GaN, AlN and their alloys.

2.2 Material Properties

Although AlN, GaN and InN can exist in the cubic zincblende (β) phase, only the hexagonal wurtzite (α) phase is thermodynamically stable. In the wurtzite phase, group III nitrides form a continuous alloy system with

direct bandgaps. In Fig. 2.1 the bandgap energies of AlN, GaN, and InN are shown as a function of lattice constant. It can be seen from the figure that InGaN alloys cover the whole visible range.

The large bandgap difference of 2.72 eV at 300 K between AlN and GaN leads to a large conduction band offset which makes it possible to achieve ISBT energies of up to 1 eV. Nitride structures are usually grown on SiC-6H (silicon carbide) or Al_2O_3 (sapphire) substrates. With lattice constants a_0 of 3.0806 Å for SiC-6H and 2.748 Å for Al_2O_3, both substrates are not lattice matched to GaN or AlN, which causes a compressive strain of the epilayer. Due to the 30° cell rotation between GaN and sapphire, an inplane lattice constant of $a_{sap}/3 = 4.759/3 = 2.748$ has to be considered for the lattice mismatch of GaN on sapphire. Recently, GaN substrates became commercially available, but they are rarely used due to their high costs and high defect density in the range of 106 cm^{-2}.

2.3 Crystalline Structure

The wurtzite crystal structure consists of alternating ABAB sequences of bilayers made of two closely spaced hexagonal layers of Ga and N atoms in the c-direction [0001],as seen on the left of Fig. 2.2. The height of the hexagonal prism c_0 and the internal parameter u_0, defined as the anion-cation bond length along the [0001] axis. The ratio u_0/c_0 is a measure of the non-ideality of the actual crystal in comparison to an ideal wurtzite structure with $u_0/c_0 = 3/8 = 0.375$. As seen on the right panel of Fig. 2.2

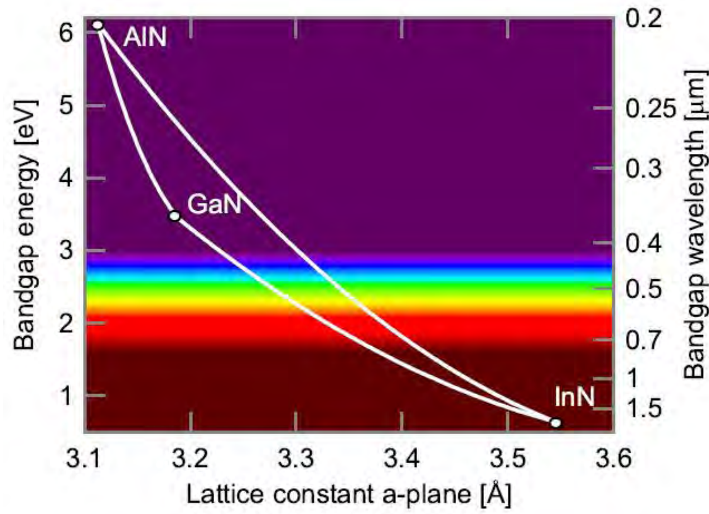

Figure 2.1: Bandgap versus lattice constant for group III nitrides.

showing the unit cell of GaN, u_0 and c_0 are directly related: the longer u_0 is, the greater is c_0. Thus, the ratio c_0/a_0 is another measure for the crystal non-ideality and equals (8/3) = 1.633 for an ideal wurtzite crystal.

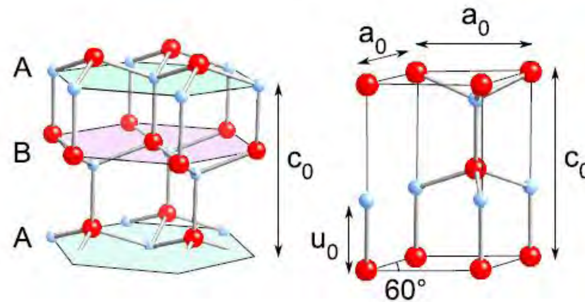

Figure 2.2: Left: hexagonal structure of wurtzite GaN with A, B bilayers. Right: wurtzite GaN unit cell. Ga-atoms are red (dark), N-atoms are blue (bright). c_0 and a_0 are the lattice constants, u_0 is the anion-cation bond length.

A wurtzite structure is asymmetric in the [0001] direction, which by convention is given by the vector pointing from the cation (Ga, Al, In) to the nearest neighbor anion (N) in positive c-direction. As seen in Fig. 2.3, the closely spaced bilayers {0001} are different in the [0001] and the [000$\bar{1}$] direction. Ga-face and N-face GaN have different chemical properties; the latter has a rougher surface [33], which is also easily attacked chemically than Ga-face GaN [34]. The crystal face depends on several factors such as substrate preparation and growth conditions.

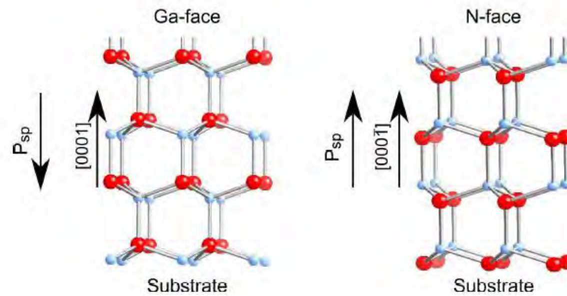

Figure 2.3: Left: Ga-face crystal in the [0001] direction. Right: N-face crystal in the [0001] direction. Ga-atoms are red (dark), N-atoms are blue (bright).

2.4 Electrical and Optical Parameters

Wurtzite phase AlN, GaN, and InN are direct bandgap semiconductors and their conduction band minima lie in the Γ valley. The direct bandgap energy of GaN was already measured in the seventies. Several groups have calculated the bandstructure of nitrides, and as already mentioned, there is still a discrepancy in the literature concerning some material parameters.

The temperature dependence of the bandgap energy E_g can be approximated by the Varshni formula,

$$E_g(T) = E_g(0) - \frac{\alpha T^2}{T + \beta} \tag{2.1}$$

using the Varshni coefficients α and β [35].

The Γ valley bandgap energy for $Al_xGa_{1-x}N$ can be approximated by a parabolic dependency on the Al content x,

$$E_g(x) = (1 - x)E_g(\text{GaN}) + xE_g(\text{AlN}) - x(1 - x)b \tag{2.2}$$

where the values of the bowing parameter b found in literature vary from 0.53 to 1.5 eV. In this work, the value of b has been taken as 0.7 eV as suggested in [35].

There is still some uncertainity about the value of the band offset at a GaN/AlN heterostructure. Bernardini and Fiorentini calculated the type I valence band offset (VBO) as function of strain for an AlN layer strained on GaN, and for a GaN layer strained on AlN [36]. In the first case they found a VBO of 0.2 eV which leads to a CBO of 2.54 eV at 0 K. In the second case, they found a VBO of 0.85 eV which leads to a CBO of 1.89 eV. A detailed experimental study of ISB absorption in GaN/AlN SL was conducted by Tchernycheva et al. [2006], where a CBO of 1.65 – 1.75 eV resulted in the

best fit to the measured data. In this work, we have taken the CBO as the function of bandgap difference of the materials. For conduction band simulations, a CBO is taken to be 65% of the bandgap difference, which is also consistent with the experimentally obtained data.

The effective mass (m^*) of the material is an important parameter for its analysis. As other parameters, there has been a great discrepancy in the reported values of m^*. The uncertainty is so high that, different values of m^* has been obtained from the same set of materials from different experiment due to the difference of growth mechanism and substrate material. The mismatch of lattice constant plays a vital role here, may cause crystal dislocation. As reported in [37], electron effective mass of GaN is $0.18m_0$ using Shubnikov-de Haas (SdH) oscillations for $Al_xGa_{1-x}N$ heterostructure. The SdH effect, quantum oscillations in the magnetoresistance, has long been an effective tool for the measurement of the properties of electrons in semiconductors and in 2DEGs in general. It has been used to determine both $m*$ in a variety of materials. When GaN is strained on AlN layer, most of the experimental results shows that electron effective mass is $\sim 0.2m_0$. Again, the electron effective mass for AlN is used $0.30m_0$ and Vegard's law is used to determine the effective mass for ternary alloys.

In Table 2.1, some of the electro-optical parameters are listed, which have been used for the analysis.

Table 2.1: Electro-optical material parameters

Parameter	GaN	AlGaN	AlN	Ref
Bandgap, E_g	3.438	$6.25x + 3.438(1 - x) + 0.7x(1 - x)$	6.25	[35]
Effective mass, m^*	0.18	$0.30x + 0.18(1-x)$	0.30	[35]
Refractive index, n	2.335	$0.431x^2 - 0.735x + 2.335$	–	[38]
Permittivity, ϵ_∞	5.31	–	4.35	[38]
Permittivity, ϵ_{steady}	10.2	$9.32x + 10.2(1 - x)$	9.32	[38]
Varshni Parameter, α	0.99×10^{-3}	–	1.799×10^{-3}	[35]
Varshni Parameter, β	830	–	1462	[35]

2.5 Polarization and Electric Field

In the absence of an external electrical field and of any deformation due to stress, the hexagonal wurtzite phase exhibits an electrical polarization along the [0001] axis which is called spontaneous polarization (P_{sp}). At the microscopic scale this means that the centers of gravity of charges of opposite signs (positive for metal atoms and negative for Nitrogen) within an unit cell do not coincide, resulting in a parallel orientation of dipoles in the [0001] directions. Group III nitrides lack an inversion symmetry along the c-axis and are therefore polar crystals and hence, they are pyroelectric. Pyroelectric phenomena are associated with a change of P_{sp} due to a change in temperature. For AlN, the change of P_{sp} with temperature is $P_{\text{sp}}/dT = 7.5\ \mu\text{C/K/m}^2$. This comparably small value is an advantage

for high power and high-temperature applications. The magnitude of P_{sp} depends on the non-ideality of the crystal (ratio u_0/c_0) and increases from GaN to AlN. The spontaneous polarization in C/m^2 for the $Al_xGa_{1-x}N$ alloy as a function of the Al content x can be approximated by [39]

$$P_{\mathrm{spAlGaN}}(x) = -0.090x - 0.034(1-x) + 0.021x(1-x). \qquad (2.3)$$

Wurtzite group III nitrides exhibit an additional piezoelectric polarization (P_{piezo}) when stress is applied. As GaN, AlN, and InN have different lattice constants and are not lattice matched to the sapphire substrate, strain induced piezoelectric polarization occurs in almost all group III nitride heterostructures, which is up to ten times larger than that in other III-V compounds.

Often the piezoelectric constants $e_{kl} = d_{kj}C_{jl}$ and not the piezoelectric moduli d_{kj} are used to describe piezoelectric properties of group III nitrides. Due to the symmetry of the wurtzite crystal, there are only three independent piezoelectric constants e_{33}, e_{31} and e_{15}. Here, e_{15} is caused by shear stress and is not further discussed, since P_{piezo} is not related to it. Using the relations

$$e_{31} = (C_{11} + C_{12})d_{31} + C_{13}d_{33}, \qquad (2.4)$$

$$e_{33} = 2C_{13}d_{31} + C_{33}d_{33}, \qquad (2.5)$$

the piezoelectric polarization can be written as

$$P_{\text{piezo}} = e_{33}\epsilon_z + e_{31}(\epsilon_x + \epsilon_y). \quad (2.6)$$

For biaxial strain, the use of the elastic constants C_{13} and C_{33} leads to

$$P_{\text{piezo}} = 2\frac{a - a_0}{a_0}\left(e_{31} - e_{33}\frac{C_{13}}{C_{33}}\right). \quad (2.7)$$

for the wurtzite phase.

The parameters used for the calculation of polarization are listed in Table 2.2.

Table 2.2: Polarization calculating parameters

Parameter	**GaN**	**AlGaN**	**AlN**	**Ref**
P_{sp}	-0.034	$-0.090x - 0.034(1-x) + 0.021x(1-x)$	-0.090	[38]
P_{piezo}	$2\frac{a-a_0}{a_0}\left(e_{31} - e_{33}\frac{C_{13}}{C_{33}}\right)$	$-0.0525x + 0.0282x(1-x)$	$2\frac{a-a_0}{a_0}\left(e_{31} - e_{33}\frac{C_{13}}{C_{33}}\right)$	[38]
e_{31}	-0.527	–	$-.536$	[35]
e_{33}	0.895	–	1.561	[35]
C_{13}	106	–	108	[35]
C_{33}	398	–	373	[35]
a_0	3.189	–	3.112	[35]

The term $(a-a_0)/a_0$ refers to the strain of the layer, where a_0 is the unstrained

lattice constant and a is the strained lattice constant. The strained lattice constant can be calculated by

$$a = \frac{\sum_j \frac{C_j \omega_j}{a_j}}{\sum_j \frac{C_j \omega_j}{a_j^2}}. \tag{2.8}$$

Here, the equation of C_j is given in [40] in terms of elastic constants for strain by

$$C_j = d_{11} + d_{12} - 2d_{13}^2/d_{33}. \tag{2.9}$$

The values of d_{kl} are listed in Table 2.3 from [40].

Table 2.3: Elastic constants for Strain

Parameter	**GaN**	**AlN**
d_{11}	390×10^9	396×10^9
d_{12}	145×10^9	137×10^9
d_{13}	106×10^9	108×10^9
d_{33}	398×10^9	373×10^9

Due to the larger lattice constant of GaN in comparison to AlN, GaN grown pseudomorphically on AlN is compressively strained, whereas AlN grown pseudomorphically on GaN is tensile strained as shown in Fig. 2.4. P_{sp} remains negative for any x Al-content. However, P_{piezo} is always positive for GaN due to tensile strain and negative for AlN layers due to compressive strain. The magnitude of P_{piezo} increases with strain, and is thus a function of the lattice mismatch.

The existence of both built-in polarization fields P_{sp} and P_{piezo} in wurtzite III-Nitride semiconductors leads to energy band bending. The electro-

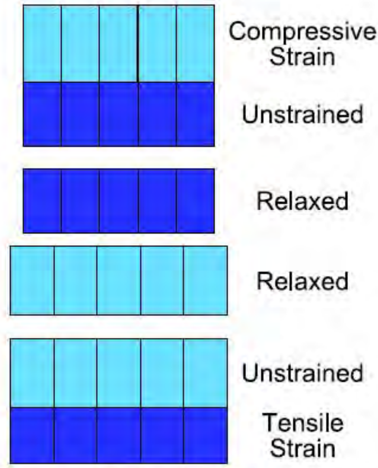

Figure 2.4: Sketch of a pseudomorphically grown layer under compressive strain (top panel) and tensile strain (bottom panel).

static fields in each layer j-th as a result of total polarization fields can be expressed as [41]

$$E_j = \frac{\sum_k (P_k - P_j)\frac{l_k}{\epsilon_k}}{\epsilon_j \sum_k \frac{l_k}{\epsilon_k}}, \tag{2.10}$$

where P is the total macroscopic polarization, ϵ is the static dielectric constant, and l is the thickness of each layers (k-th, j-th). The subscripts k and j correspond to the k-th and j-th layers.

We note that to ensure zero average electric field in the layers, note that the electric field expression in Eq. (2.10) needs to satisfy the periodic boundary conditions [41]

$$\sum_j l_j E_j = 0. \tag{2.11}$$

2.6 Results and Discussion

With the developed material library for nitride materials, a number of structures have been solved for wavefunctions and quantized energy values. The simulation conduction band profiles are shown in this chapter, starting from simple binary superlattice to complete QCD design.

2.6.1 AlN/GaN Superlattice

Two AlN/GaN superlattice structure with alternating GaN quantum wells and AlN barriers have been studied. The well (and barrier) widths for two structures were 15 Å (and 15 Å) and 30 Å (and 30 Å). The QW doping level is 10^{20} cm^{-3} and the structures are strained to an AlN buffer, giving rise to piezoelectric polarizations in the GaN QWs only. In this case, electron effective mass (m^*) is taken to be $0.20m_0$ [38].

The solved band structure for 15 Å stucture is shown in Fig. 2.5. The reported simulation result simulated using *cband* self-consistent simulation [38] is compared with our simulation result using QCL Simulation Package. The mismatch between the two results is about 3% where the reported value of the difference of two energy state is 0.90 eV.

In Fig. 2.6, our simulation result of a 30 Å superlattice structure using QCL Simulation Package is presented. Table 2.4 lists the solved energy values found from the two approaches.

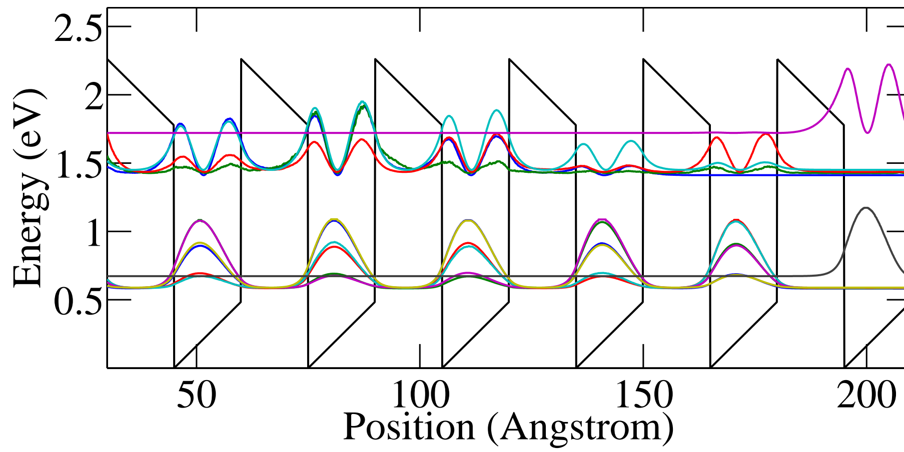

Figure 2.5: QCL Simulation results of 15 Å AlN/GaN superlattice.

Table 2.4: Energy values between different energy levels

Energy State	Reported value	Simulation result	Mismatch
1-2	0.46 eV	0.47 eV	2%
2-3	0.48 eV	0.49 eV	2%
3-4	0.51 eV	0.53 eV	3.5%

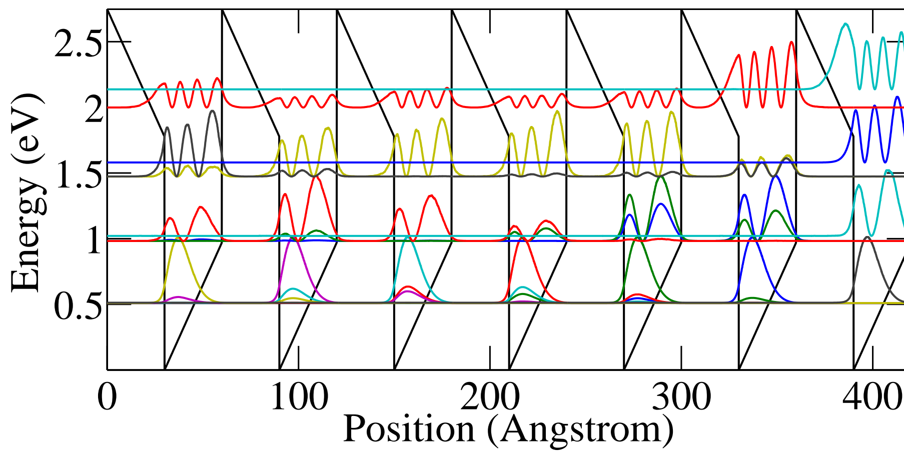

Figure 2.6: QCL Simulation results of 30 Å AlN/GaN superlattice.

2.6.2 Quantum Cascade Detector (QCD)

A GaN/AlN QCD design with an ISBT energy of 600 meV also reported in [38]. The active region consists of a 26 Å thick active GaN QW n-type doped to 10^{19} cm^{-3} followed by an extraction cascade formed by a regular SL with undoped 12.5 Å thick GaN QWs and AlN barriers. All layers are strained on a 50% $Al_xGa_{1-x}N$ buffer. The electron effective mass is considered $0.18m_0$[37] due to the buffer layer.

Figure 2.7 shows the simulation results, depicting ISBT energy of 571 meV which is about 3.5% mismatch from the reported value.

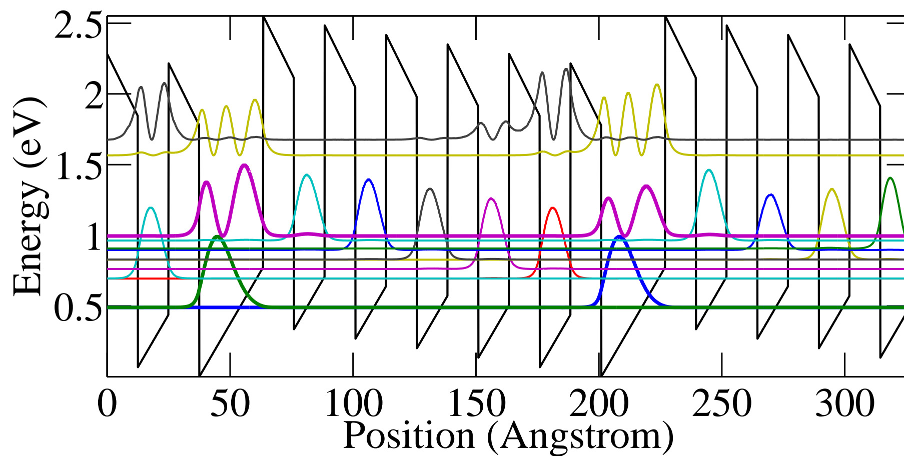

Figure 2.7: QCL Simulation Package results of AlN/GaN superlattice QCD.

In another paper [4], a quantum cascade detector (QCD) in the GaN/ AlGaN/ AlN material system was implemented. The design takes advantage of the large internal field existing in the nitrides in order to generate the

essential saw tooth energy level structure. A stage of a QCD is composed of a quantum well (QW) which absorbs the desired wavelengths in the active region, followed by several QWs in which the confined energy levels form a staircase, so that optically excited carriers can be extracted from one active region to the next. A cascade of such stages results in a charge separation over a large distance enhancing the photo-response which depends on the number of stages. The sample was grown by plasma-assisted molecular beam epitaxy on a 1-μm-thick AlN layer. The structure consists of 40 periods of a 6 ML thick GaN quantum well followed by a supeer-lattice structure consisting of 5 periods of Al/$Al_{0.25}Ga_{0.75}N$ (4 ML/ 4 ML). N-type doping (Si) was introduced in the GaN QWs at a nominal level of 5×10^{18} cm^{-3}. The reported energy separation between two energy level is 0.75 eV and it forms 92 meV ladder type energy band in between two periods. Our simulation results, which is shown in Fig. 2.8, suggests almost accurate result to the reported value, which is about 1% mismatch.

2.6.3 Quantum Cascade Laser (QCL)

Designs of GaN/AlGaN quantum-cascade lasers emitting at 34 and 38 μm (ΔE = 36 and 34 meV) are presented, assuming either a- or c-plane crystal growth orientation. In the calculation of the quasibound state energies and wave functions, we account for the intrinsic electric field induced by piezoelectric and in case of c-plane growth, the spontaneous polarization.

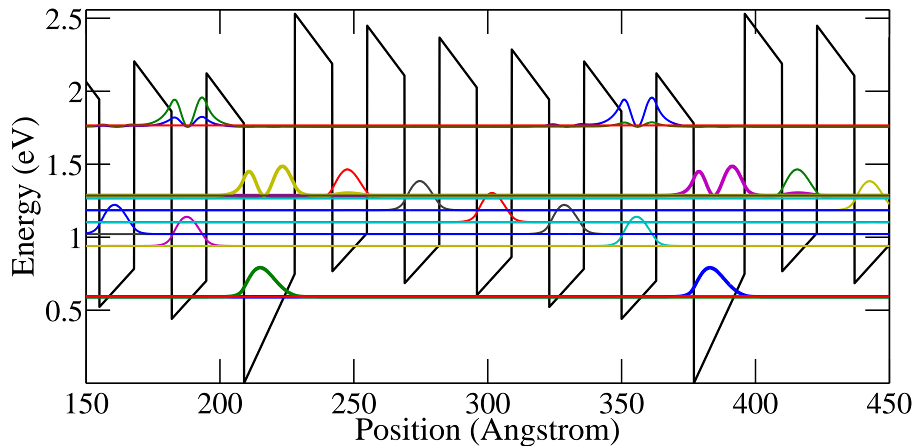

Figure 2.8: QCL Simulation Package results of AlN/GaN superlattice QCD designed to operate at 1.7 μm.

The intrinsic property of GaN-based structures grown along the main symmetry direction (c-plane) is a large electric field induced by piezoelectric and spontaneous polarization, which significantly alters the conduction band profile. On the other hand, the a-plane crystal orientation cancels the spontaneous polarization and therefore considerably lowers the intrinsic electric field strength, making the design less sensitive to polarization field parameter variations. In our simulations, we have taken into account the piezoelectric-induced electric field for both a- and c-plane cases, and the spontaneous polarization-induced field for the c-plane growth, and modeled it using electrostatic boundary conditions at the interfaces and periodic boundary condition across the structure. The electronic and optical properties of GaN-based multiple quantum well (QW) structures are very much influenced by the intrinsic electric field, which makes the design of complex quantum structures a highly challenging task.

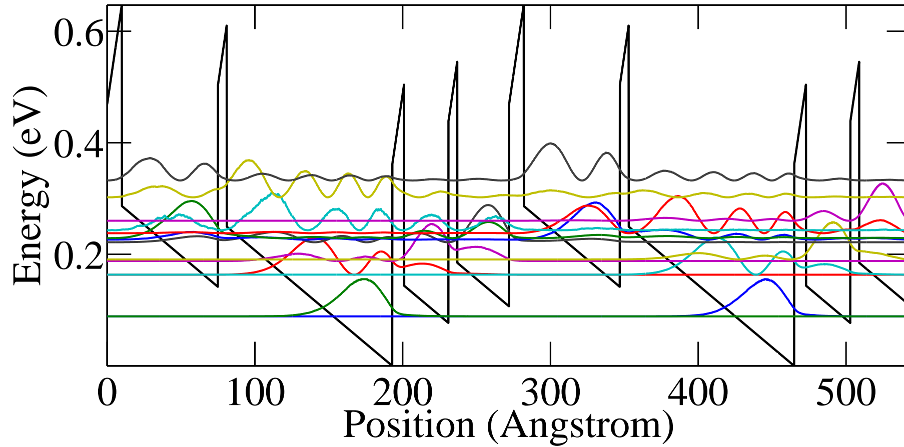

Figure 2.9: QCL Simulation results of conduction band profile of c-plane design of a THZ QCL.

The simulation results are presented in Fig. 2.9 and Fig. 2.10. Figure 2.9 gives the c-plane design of QCL. Our simulation gives the energy difference of two lasing level 34.9 meV, which only 2.5% deviated from the reported design value. In the second design (a-plane design), our result is even more accurate. The energy separation of the lasing levels in this case is 36.4 meV, which gives deviation of only 1% from reported value. The band structure for a-plane design is presented in Fig. 2.10.

2.7 Summary

The summary of this chapter can be given by the following points,

- Material properties and crystalline structure of nitride material are

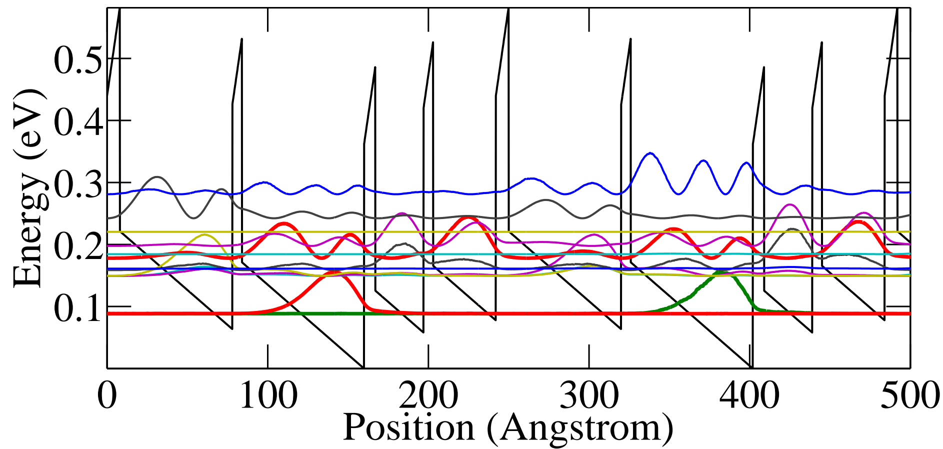

Figure 2.10: QCL Simulation Package results of conduction band profile of a-plane design of a THZ QCL.

presented.

- Electrical and optical parameters of nitride material are listed. This material library is used to simulate the wavefunction of nitride superlattice structure.

- We incorporated the internal electric field and polarization of nitride to develop the material library. All together, we developed a simulator tool for nitride based superlattice structure.

- The verification of the simulator is presented in this chapter. The mismatch between developed simulator and reported values was found below 5%. Different reported structures were used for this verification.

Chapter 3

Theoretical Framework

3.1 Introduction

The purpose of this chapter is to outlay the relevant physics of intersubband transitions in semiconductors and the description of photodetectors in general. These two subjects are the base of a successful description and characterization of quantum cascade detectors.

3.2 Intersubband Transitions in Quantum Wells

The description of the intersubband absorption is the first point in the modeling of a photodetector based on intersubband transitions. In the framework of a single-particle description in one single baud of the electronic structure of the bulk semiconductor, it is possible to calculate the intersubband absorption coefficient based on Fermi's golden rule for the induced transition rate. The description below follows the description by

Helm [42] with additional information and parts of the nomenclature as in Bastard [43].

According to the well known Bloch description of the electronic structure of a bulk crystal, we start by stating that the internal potential must be periodic with the lattice structure of the crystal. Therefore, the wavefunction $\psi_i(\vec{r})$ for a single electron in the conduction band of the semiconductor is written as the product of an envelope function $f_i(\vec{r})$, supposed to vary slowly over the distance of a lattice period, and a function $u_v(\vec{r})$, is periodic with the lattice,

$$\psi_i(\vec{r}) = f_i(\vec{r})u_v(\vec{r}). \tag{3.1}$$

In the case of a bulk crystal, the envelope functions are simply plane waves $f_i(\vec{r}) = e^{i\vec{k}_i\cdot\vec{r}}$. In the presence of an external potential, like quantum wells due to material composition modulation, or an applied electric field, the envelope function $f_i(\vec{r})$ needs some more degree of freedom. Assuming that the Bloch function $u_v(\vec{r})$ is identical in all material compositions, the Schrödinger equation for the envelope function $f_i(\vec{r})$ can be written as

$$\frac{-\hbar^2}{2m^*}\nabla^2 f_i(\vec{r}) + V(\vec{r})f_i(\vec{r}) = E_i f_i(\vec{r}). \tag{3.2}$$

If we further assume that the materials are bulk in the two directions x and y of $\vec{r} = (x, y, z)$ with z being the growth direction, the envelope function

can be further separated with the ansatz

$$f_{nk_\perp}(\vec{r}) = \frac{1}{\sqrt{A}} e^{i\vec{k_\perp}\cdot\vec{r}} \varphi_n(z), \tag{3.3}$$

with $\vec{k_\perp}$ the vector $(k_x, k_y) = (k_x, k_y, 0)$ in the x - y plane and $V(\vec{r}) = V(z)$ only varying along z. As $\vec{k_\perp} \cdot \vec{r} = k_x x + k_y y$ does not depend on z, inserting Eq. (3.3) into Eq. (3.2) we get

$$\frac{-\hbar^2}{2m^*}\varphi_n(z)\left(\frac{d^2}{dx^2} + \frac{d^2}{dy^2}\right)e^{i\vec{k_\perp}\cdot\vec{r}} + \frac{-\hbar^2}{2m^*}e^{i\vec{k_\perp}\cdot\vec{r}}\frac{d^2}{dz^2}\varphi_n(z) + e^{i\vec{k_\perp}\cdot\vec{r}}V(z)\varphi_n(z) = E_{n,k_\perp}e^{i\vec{k_\perp}\cdot\vec{r}}\varphi_n(z). \tag{3.4}$$

Equation (3.4) leads to the one-dimensional Schrödinger equation along the z axis

$$\frac{-\hbar^2}{2m^*}\frac{d^2}{dz^2}\varphi_n(z) + V(z)\varphi_n(z) = E_n\varphi_n(z). \tag{3.5}$$

The total energy eigenvalues are then

$$E_{n,\vec{k_\perp}} = E_n + \frac{\hbar^2 \vec{k_\perp^2}}{2m^*} \tag{3.6}$$

with only the subband energies E_n depending on the shape of $V(z)$. In general, the effective mass m^* will not be the same in two different materials A and B building an interface at $z = z_{AB}$. Therefore, Eq. (3.5) has to be solved in each material layer with the boundary conditions

$$\varphi_n^A(z_{AB}) = \varphi_n^B(z_{AB}) \quad \text{and} \quad \frac{1}{m^{*A}}\frac{d\varphi_n^A}{dz}(z_{AB}) = \frac{1}{m^{*B}}\frac{d\varphi_n^B}{dz}(z_{AB}) \tag{3.7}$$

to ensure that the wavefunction is continuous and the probability current

is conserved across the interface. Equation (3.5) can only be solved analytically for the most simple cases, like one finite and symmetric quantum well. Generally, numerical methods are used, e. g., the finite difference matrix (FDM) method. Within the scope of this work, the software "QCL Simulation Package" written by Dr. Muhammad Anisuzzaman Talukder was used. This package is an implementation of the finite difference matrix method mentioned before, combined with a Poisson solver to allow for a self-consistent Coulomb potential and the inclusion of nonparabolicity for several material systems.

3.3 Absorption Coefficient of a Single Quantum Well

For the absorption coefficient, we used Fermi's golden rule to calculate the transition rate from an initial state i to a final state f with the interaction Hamiltonian $H' = e/2m^*(\boldsymbol{A} \cdot \mathbf{p} + \boldsymbol{p} \cdot \boldsymbol{A})$ under the influence of an external electromagnetic field. The rate is given by

$$W_{if} = \frac{2\pi}{\hbar} |\langle \psi_i | H' | \psi_f \rangle|^2 \delta(E_f - E_i - \hbar\omega). \tag{3.8}$$

In our case of one-band effective-mass model, the interaction is correctly described by using the effective mass m^* in the expression above for H'.

The incident electromagnetic wave is described by the plane wave

$$E(\vec{r},t) = E_0 e \cos(\vec{q}\cdot\vec{r} - \omega t) = \frac{E_0 e}{2}\left(e^{i(\vec{k}\cdot\vec{r}-\omega t)} + e^{-i(\vec{k}\cdot\vec{r}-\omega t)}\right), \tag{3.9}$$

where $E(\vec{r},t)$ is the electric field as function of position and time, $\vec{q}$ the propagation vector, and $\boldsymbol{e}$ the linear polarization vector perpendicular to $\vec{q}$. We choose a gauge in which the associated electrical potential ϕ is zero, producing the electric field by $E = \frac{-\partial A}{\partial t}$. and set the vector potential $\boldsymbol{A}$ as

$$\boldsymbol{A}(\vec{r},t) = \frac{E_0 e}{\omega}\sin(\vec{q}\cdot\vec{r} - \omega t) = \frac{iE_0 e}{2\omega}e^{i(\vec{q}\cdot\vec{r}-\omega t)} + c.c. \tag{3.10}$$

We can further apply the dipole approximation, which necessitates that the characteristic length of the electronic system is much smaller than the wavelength of the radiation. This is very well fulfilled, as the wavelength is of the order of several micrometers and widths of quantum wells are typically tens of nanometers. Under this approximation, $\boldsymbol{A}$ and $\boldsymbol{p}$ commute, which simplifies the interaction Hamiltonian to $H' = (e/m^*)\boldsymbol{A}\cdot\boldsymbol{p}$. Inserting it into Eq. (3.8), we obtain

$$W_{if} = \frac{2\pi}{\hbar}\frac{e^2E_0^2}{4m^{*2}\omega^2}|\langle\varphi_i|\boldsymbol{e}\cdot\boldsymbol{p}|\varphi_f\rangle|^2\delta(E_f - E_i - \hbar\omega). \tag{3.11}$$

Inserting the envelope function expression from Eq. (3.1) into the matrix element $\langle\varphi_i|\boldsymbol{e}\cdot\boldsymbol{p}|\varphi_f\rangle$ and taking advantage of the fact that the Bloch functions $u_v(\vec{r})$ vary rapidly over $\vec{k}_\perp^{-1}$ leads to

$$\langle\varphi_i|\boldsymbol{e}\cdot\boldsymbol{p}|\varphi_f\rangle = \boldsymbol{e}\cdot\langle u_v|\boldsymbol{p}|u_{v'}\rangle\langle f_n|f_{n'}\rangle + \boldsymbol{e}\cdot\langle u_v|u_{v'}\rangle\langle f_n|\boldsymbol{p}|f_{n'}\rangle, \tag{3.12}$$

which splits the optical transitions into two types. The first term describes the interband transitions and the second term describes the intersubband transitions. In the case of an interband transition, the band indices of the initial and final state v and v' are different, so the overlap integral of the Bloch functions, $\langle u_v | u_{v'} \rangle$ vanishes and only the first term remains. If the final and initial states are in the same band, $v = v'$ makes the first term vanish and $\langle u_v | u_{v'} \rangle = 1$. The remaining dipole matrix element of the envelope functions $\langle f_n | \boldsymbol{e} \cdot \boldsymbol{p} | f_{n'} \rangle$ describes the optical intersubband transition.

3.4 Detector Physics

3.4.1 Zero Bias Resistance (R_0A)

As usual with detector kind of devices, the resistance will be presented in terms of R_0A, where R_0 is the resistance of the pixel and A the area of the pixel. Hypotheses about electronic transitions between the different energy levels have to be made for the determination of the R_0A of such a structure. Considering the well and barrier widths, only interactions between electrons and longitudinal optical phonons (LO-phonons) have been taken into account [44]. The differences between the energy levels are indeed sufficiently large to neglect the influence of the interaction between electrons and acoustical phonons. All other possible interactions have been neglected as well. Interface roughness has low influence on intersubband scattering, although it was possible to measure its influence at very low temperature (4 K).

The transition rates due to the interaction between electrons and optical phonons will be evaluated first following Ferreira and Bastard [45]. Starting from an initial state of wave vector k and energy E in the subband i, the transition rate $S_{ij}^{a,e}(E)$ towards the subband j (in s^{-1}) is obtained through the integration of a matrix element involving a standard electron-optical-phonon Hamiltonian. This integration involves all the possible final states of energy $E \pm \hbar\omega_{\mathrm{LO}}$ in the subband j, where $\hbar\omega_{\mathrm{LO}}$ is the energy of a LO phonon, the $\pm$ sign accounting for absorption or emission of LO phonons, corresponding to superscript a or e, respectively. Transition rates S_{ij}^{a} and S_{ji}^{e} are are related to each other by

$$S_{ij}^{a}(E) = S_{ji}^{e}(E + \hbar\omega_{\mathrm{LO}}). \tag{3.13}$$

Finally, the global transition rate G_{ij} between the subband i and subband j is the sum of the two transition rates for absorption of LO phonons G_{ij}^{a}, and emission of LO phonons G_{ij}^{e}. In order to calculate the global transition rates G_{ij}^{a} and G_{ij}^{e}, all the initial states of energy E are filled at thermal equilibrium by the Fermi-Dirac occupation factor f. The global absorption and emission transition rates are given by

$$G_{ij}^{a} = \int_{\epsilon_j - \hbar\omega_{\mathrm{LO}}}^{\infty} S_{ij}^{a}(E) f(E)[1 - f(E + \hbar\omega_{\mathrm{LO}})] n_{\mathrm{opt}} D(E) dE, \tag{3.14}$$

$$G_{ij}^{e} = \int_{\epsilon_j - \hbar\omega_{\mathrm{LO}}}^{\infty} S_{ij}^{e}(E) f(E)[1 - f(E - \hbar\omega_{\mathrm{LO}})](1 + n_{\mathrm{opt}}) D(E) dE. \tag{3.15}$$

Here, n_{opt} is the Bose-Einstein statistic function which accounts for phonon

population, $D(E)$ is the two-dimensional density of states of subband i, and ϵ_j is the minimum of the energy of the subband j. Transition times τ_{ij} can be deduced from the global transition rate G_{ij} by

$$\tau_{ij} = n_i/G_{ij}, \tag{3.16}$$

where n_i is the two-dimensional carrier density associated with subband i.

The global current density will be evaluated by counting the electronic transitions between the two consecutive cascades. On one hand, each cascade stays at thermodynamical equilibrium, but on the other hand, equilibrium between the two consecutive cascades is broken. As a consequence, transition rates from cascade A to cascade B are not equal to the reciprocal transitions rates from cascade B to cascade A. A global current appears. This global current density is given by

$$J = q \sum_{i\epsilon A} \sum_{j\epsilon B} \left[G_{ij}(V) - G_{ji}(V) \right]. \tag{3.17}$$

Using the equation of G_{ij}^a and G_{ji}^e in the density equation and for little variations of the voltage, the difference of rates can be approximated by the following equation

$$G_{ij}^a - G_{ji}^e \approx G_{ij}^a \left(V = 0 \text{ V}\right) \frac{qV}{k_b T}. \tag{3.18}$$

A similar expression can be found for the difference

$$G_{ij}^{e} - G_{ji}^{a} \approx G_{ij}^{e}\,(V = 0\ \mathrm{V})\,\frac{qV}{k_b T}. \tag{3.19}$$

Finally the global current density is calculated by the formula

$$J = q \sum_{i\epsilon A} \sum_{j\epsilon B} G_{ij} \frac{qV}{k_b T}, \tag{3.20}$$

where the term G_{ij} is defined by the sum of G_{ij}^{a} and G_{ij}^{e} calculated without any applied voltage.

Now, the parameter, $r_0 A$ can be deduced from Eq. (3.20) as

$$r_0 A = \frac{k_b T}{q^2 \sum_{i\epsilon A} \sum_{j\epsilon B} G_{ij}}. \tag{3.21}$$

The whole resistance of the device is directly proportional to the number of periods N. The overall zero bias resistance of the device can be calculated as

$$R_0 A = N r_0 A. \tag{3.22}$$

3.4.2 Absorption

The absorption coefficient α is defined as the ratio of electromagnetic energy being absorbed per volume and time, and the intensity of incident light I. In the case of a quasi-two-dimensional system like the 2D electron gas in the quantum well, it is more common to define a 2D absorption

coefficient α_{2D} by calculating the ratio of absorbed energy per area (A) and time, and the intensity. The absorption coefficient can be written as [46],

$$\alpha_{2D} = \sum_{i\epsilon A}\sum_{j\epsilon B} \frac{q^2 z_{ij}^2 \omega^2}{nc\epsilon_0} \frac{\Gamma_{ij}/2}{(E_j - E_i - \hbar\omega)^2 + (\Gamma_{ij}/2)^2} \left(N_i - N_j\right). \tag{3.23}$$

3.4.3 Quantum Efficiency

The overall quantum efficiency (η_{tot}) depends on the collection and absorption of carrier due to incident light and escape probability (p_e) of the device. The maximum achievable value of η_{tot} in a QCD include $1/N$ term due to the capture probability $p_c = 1$, with N being the number of period, the former is

$$\eta_{\text{tot}} = \eta_{\text{abs}} p_e \frac{1}{N}, \tag{3.24}$$

where η_{abs} is the absorption efficiency.

The escape probability can be calculated using the transport of carrier through the device. Starting from one of the upper states, all paths leading either to the ground state of the next period (escape) or back to the original ground state (fallback) are identified. For each of these paths going through nodes (states) $s_1, s_2, \ldots, s_n$, its probability p_{path} to be traversed by an electron is the product of the probabilities of each involved transition. It can be defined by

$$p_{\text{path}} = \prod_{i=1}^{n-1} p_{s_i \to s_{i+1}}, \tag{3.25}$$

where $p_{s_i \to s_{i+1}} = r_{s_i \to s_{i+1}} / \sum_k r_{s_i \to k}$ is the probability of exiting from state s_i to

state s_{i+l} based on all transition rates $r_{a \to b}$ from the band structure calculation. Summing the probabilities of all paths leading to the next ground state results in the simulated escape probability,

$$p_e = \sum_l p_{\text{path}l}. \tag{3.26}$$

3.4.4 Responsivity

The incident photons in a photodetector generate electrons. The number of electrons passing through the device is related to the number of photons. "The overall quantum efficiency" depends on the amount of carrier generated to the amount of incident photon. Though determining the number of electrons and photons is practically almost impossible, it is possible to estimate the amount of carrier generated for the incident of photons on the detector. Responsivity, R of the detector can be calculated with the calculated quantum efficiency and absorption of the detector [47]. It is defined by

$$R = \frac{\lambda e \eta_{tot}}{hc}, \tag{3.27}$$

where e, h, c and λ are the electron charge, the Planck's constant, the speed of light, and the wavelength of the incident light, respectively. The response of a detector such as a QCD is related to two different phenomena: The absorption of infrared photons by the active region and the extraction of the excited electrons from the upper subband to the cascade of quantum

levels. The spectral response is expressed as follows [48]

$$R(\lambda) = R_{\text{peak}} r_{\text{norm}}(\lambda). \tag{3.28}$$

The parameter, $r_{\text{norm}}(\lambda)$ is the normalized spectral response and R_{peak} is the peak responsivity, which can be expressed as

$$R_{\text{peak}} = \frac{1}{N}\frac{q\lambda}{hc}\eta_{\text{peak}}. \tag{3.29}$$

3.4.5 Detectivity

From responsivity and resistivity values, we can deduce the Johnson noise limited detectivity given by [48]

$$D^{*} = R(\lambda)\sqrt{\frac{R_0 A}{4kT}}, \tag{3.30}$$

where $R(\lambda)$ is the peak responsivity, R_0 is the device resistance at zero bias, A is the mesa area, and T is temperature of the sample.

3.5 Summary

- In this chapter, we described the procedure used to solve of wavefunctions in a quantum well. The solved wavefunctions and energy levels inside a quantum well are used for intersubband transitions. The boundary conditions for solving the wavefunctions is also discussed.

- The calculation method of absorption in quantum wells is described and scattering rates using Fermi's golden rule are calculated.

- We described the detector physics in terms of transport, zero bias resistance, quantum efficiency, absorption coefficient, and responsivity.

- A model is presented to calculate zero bias resistance (R_0A) using the intrasubband transitions. The intersubband transitions were ignored in the calculation of R_0A as it was much smaller than intrasubband transitions.

- The theoretical model of calculating responsivity of the detectors using quantum efficiency and absorption coefficient is also presented in this chapter.

Chapter 4

Results and Discussion

4.1 Introduction

In this chapter, we are going to present the results and discussion of the study of nitride based QCD having operating wavelength. We intend to present an optimized design of nitride based mid-infrared QCD along with the performance analysis of the device. The detail analysis of electrical transport, scattering mechanism and performance of the designed QCDs have been presented. The simulation of the performance was carried out using the simulator developed in Matlab for the characterization of a QCD.

4.2 Verification of Developed Simulator

This chapter presents the results and discussion of the various design studied in terms of temperature and performance. First, a study of previously reported QCD designs have been given. This study includes different

QCD designs composed of GaAs/AlGaAs, GaAs/InAlAs, and GaN/AlGaN material systems operating at wavelengths in 1 μm- 9 μm. The results are matched with the reported values to verify our developed simulator for nitride based structures. Finally, two designs of QCD have been proposed for GaN/AlGaN material system operating in the mid infrared region. The reason to attempt to design nitride based QCD for mid-infrared region is to exploit the advantage of nitride material system. Nitride material shows higher break-down voltage, electron mobility, and efficiency compared to popular material systems like GaAs and its alloys.

4.2.1 GaAs/AlGaAs QCD

The QCD considered in the paper [2] is a GaAs/AlGaAs heterostructure composed of seven quantum wells which is repeated 40 times. The quantum wells are GaAs layers with AlGaAs barriers on both sides. The first quantum well of each period is *n*-type doped in order to populate the ground state E_1 in the conduction band with electrons. We consider a doping concentration of ~5×10^{11} cm^{-2}. The alloy in the barriers is $Al_{0.34}Ga_{0.66}As$. The layer widths of the structure are 68/ **56.5**/ 20/ **39.5**/ 23/ **31**/ 28/ **31**/ 34/ **31**/ 39/ **31**/ 48/ **22.6**, where the layer sequences are given in Å, $Al_{0.34}Ga_{0.66}As$ barriers are in bold face, and GaAs wells are in normal face. The calculated band structure has been given in Fig. 4.1.

The resistivity of the quantum structure presents the noise performance of the QCD. The resistance is calculated using Eq. (3.22). The higher the

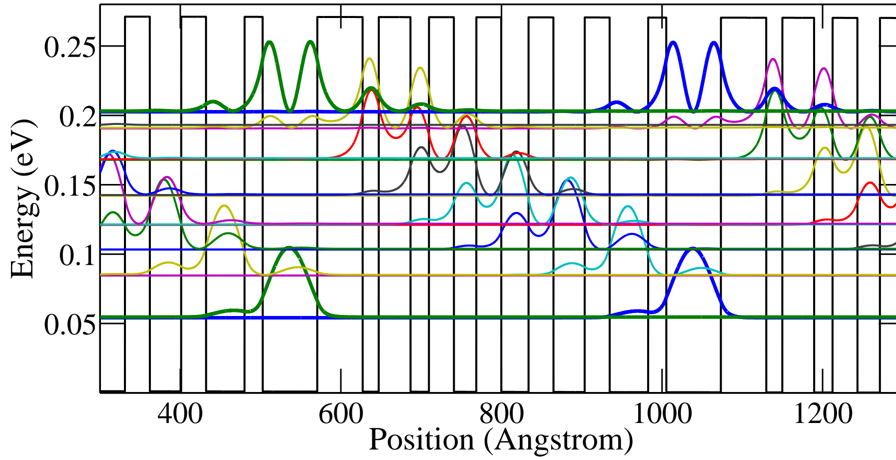

Figure 4.1: Band structure of GaAs/AlGaAs QCD operating at 9μm.

resistance the better the noise performance of the detector. This design presents relatively higher resistivity, compared to the first generation of QCDs [49].

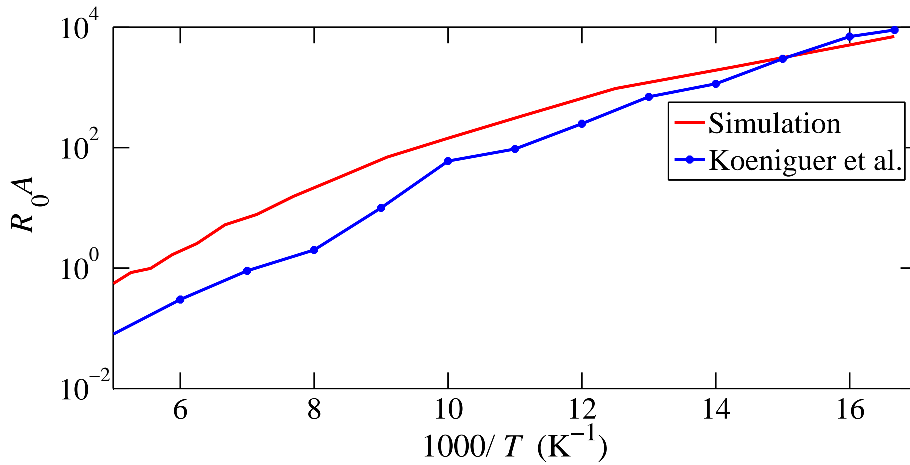

Figure 4.2: R_0A of GaAs/AlGaAs QCD operating at 9μm [2].

The absorption coefficient and responsivity are also calculated for this

QCD, and we find that the results agrees well with the experimental results presented in [2]. The absorption coefficient presented in Fig. 4.3 shows that the peak absorption is ~9.1 μm wavelength. The responsivity of the device is also shown in Fig. 4.4. It can be seen from the figure that primary peak absorption and responsivity decreases with increasing temperature, but the secondary peaks show inverted behavior, the absorption and responsivity increases with increasing temperature. This detector was designed to operate at T = 77 K and it shows very low detectivity beyond 200 K. So the study of temperature dependence was done upto 250 K for this detector.

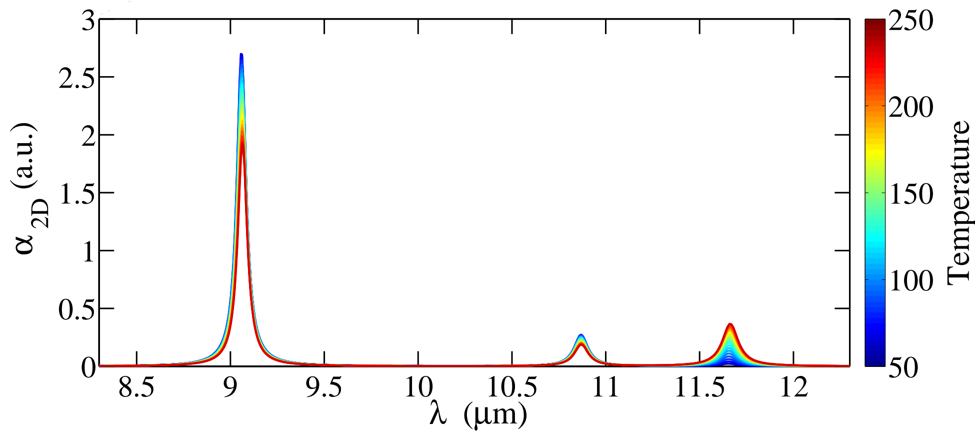

Figure 4.3: Absorption coefficient of GaAs/AlGaAs QCD designed to operate at 9μm.

4.2.2 InGaAs/InAlAs QCD

An adaptation to the mid-infrared wavelength range was taken by Gaft et al. [3] after the success of the far-infrared detector. As the energy of the

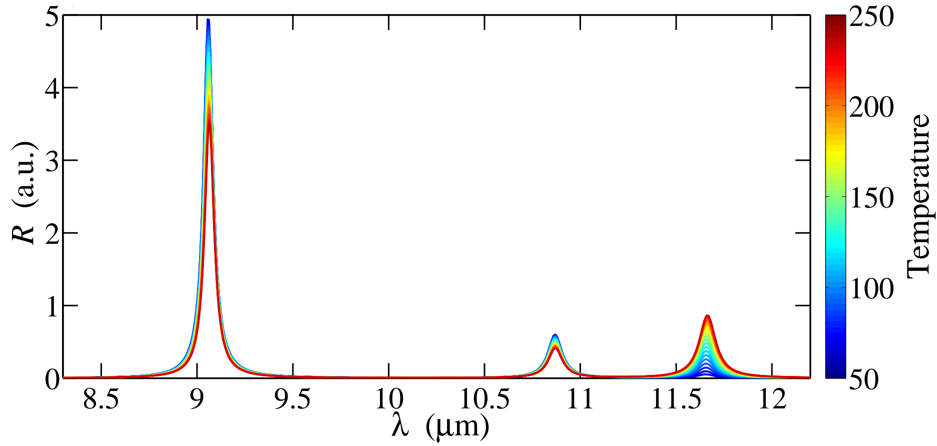

Figure 4.4: Responsivity of GaAs/AlGaAs QCD designed to operate at 9μm.

optical transitions is bigger than the energy of the LO-phonon, the extraction cascade was designed in a way that one could profit from the highly efficient electron-phonon scattering process.

Figure 4.5 shows the design of the QCD that absorbs at $\sim$ 9.1 μm. If light of resonant wavelength is incident on the detector, electrons of the ground state 0 can absorb the incident photon and be excited into one of the two upper states 7 or 8. The wells and barriers are made in InGaAs and InAlAs. The layer widths of the structure are 100/ **47**/ 39/ **25**/ 43/ **19**/ 54/ **16**/ 66/ **22.6**, where the layer sequences are given in Å, InAlAs barriers are in bold face, and InGaAs wells are in normal face.

The resistivity of the device has been calculated and presented in Fig. 4.6. This particular design showed higher resistance than the previously re-

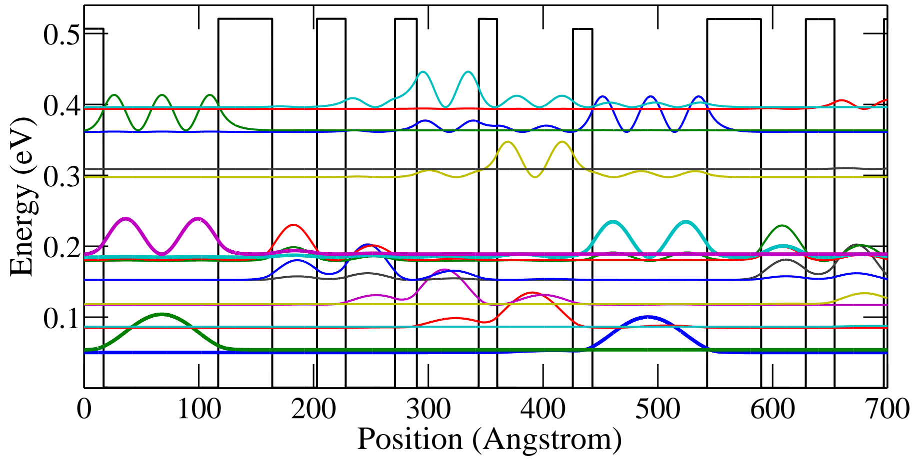

Figure 4.5: Band structure of InGaAs/InAlAs QCD operating at 9μm.

ported QCD in [44]. We note that our simulation model is well matched with the experimental value upto $T = 80$ K. Below 80 K, it shows some deviation from experimental values, but the percentage of error is very low. It verifies the developed simulator model which was later used to design nitride based QCDs.

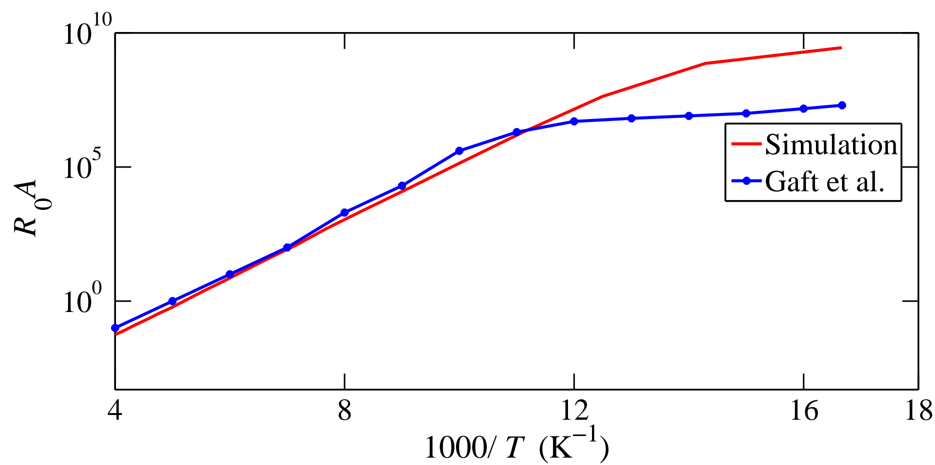

Figure 4.6: R_0A of InGaAs/InAlAs QCD operating at 9μm [3].

The absorption coefficient as shown in Fig. 4.7 is calculated using the model defined in chapter 3. The absorption coefficient of the device decreases with temperature. There is also a shift in the wavelength at which maximum absorption is achieved as the temperature increases. The effect of temperature variation is included in the solution of band structure and consequently that has effect on absorption spectrum.

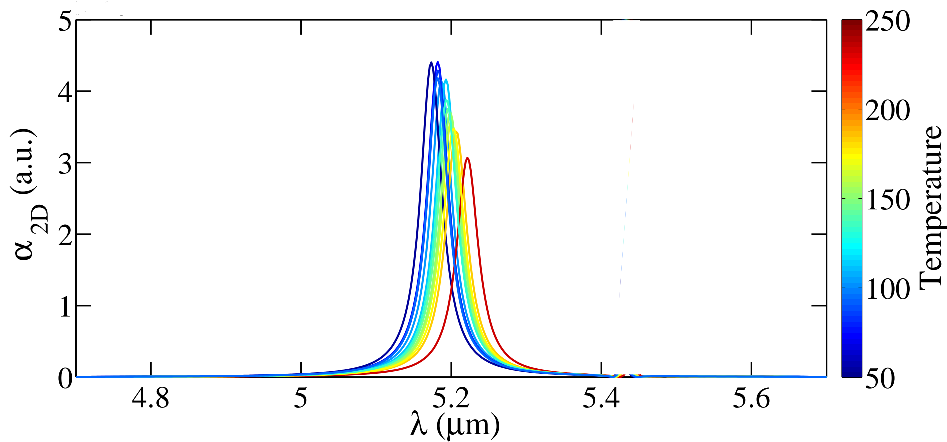

Figure 4.7: Absorption coefficient of InGaAs/InAlAs QCD operating at 9μm.

The responsivity of the device was also calculated and it was found that it matches fairly with the experimental values presented in [3]. The decrease of peak responsivity and shift of wavelength is also observed in the responsivity spectrum as it was observed in absorption spectrum. The responsivity spectrum is shown in Fig. 4.8

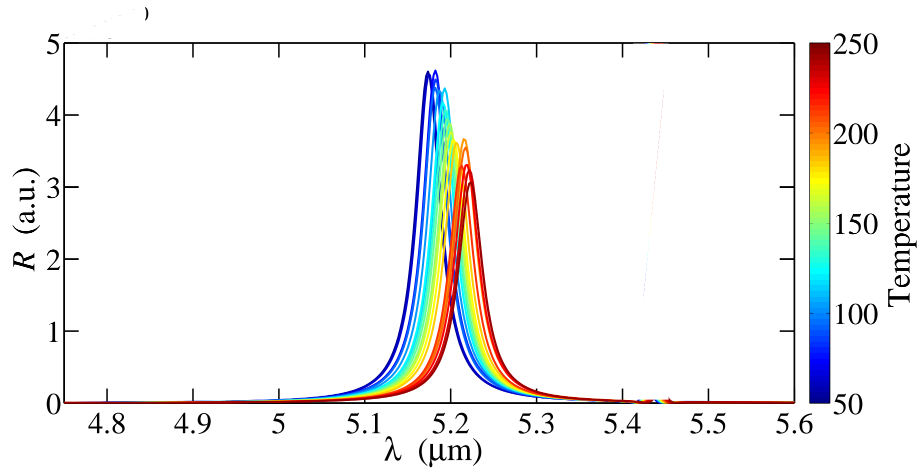

Figure 4.8: Responsivity of InGaAs/InAlAs QCD operating at 9 μm.

4.2.3 GaN/AlGaN QCD

The QCD demonstrate in [4] was grown by plasma-assisted molecular beam epitaxy on a 1 μm thick AlN layer on c-sapphire template. The structure consists of 40 periods of a 6 ML thick GaN quantum well followed by a superlattice structure consisting of of $AlN/Al_{0.25}Ga_{0.75}N$ (4 ML/4 ML). N-type doping (Si) was introduced in the GaN QWs at a nominal level of 5×10^{18} cm^{-3}.

The solved band structure of the QCD is presented in Fig. 4.9, which matches with that reported in [4].

The resistance of the QCD is calculated using Eq. (3.22) and presented in Fig. 4.10. The resistance of the nitride device is much higher than other two material system studied. The internal electric field of nitride system causes

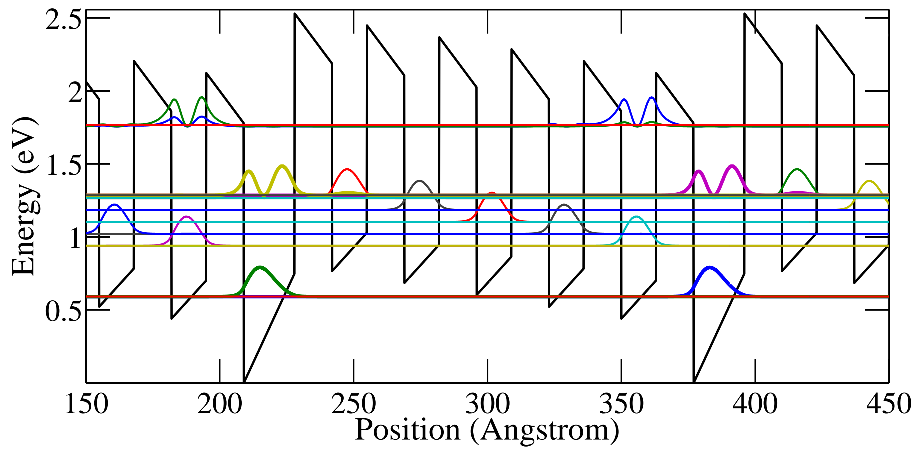

Figure 4.9: Band structure of GaN/AlGaN QCD designed to operate at 1.85 μm.

this higher resistance of the device which ensures better noise tolerance.

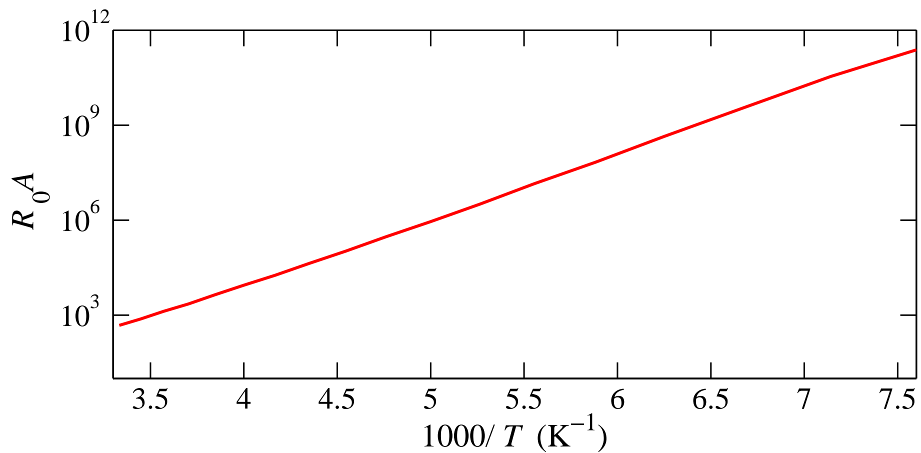

Figure 4.10: R_0A of GaN/AlGaN QCD designed to operate at 1.85 μm [4].

We also calculate the absorption coefficient of this nitride QCD as the temperature varies. We also note that the value of the coefficient decreases

with the increase of the temperature as shown in Fig. 4.11. We also note that the wavelength corresponding to peak absorption shifts due to change in the band structure.

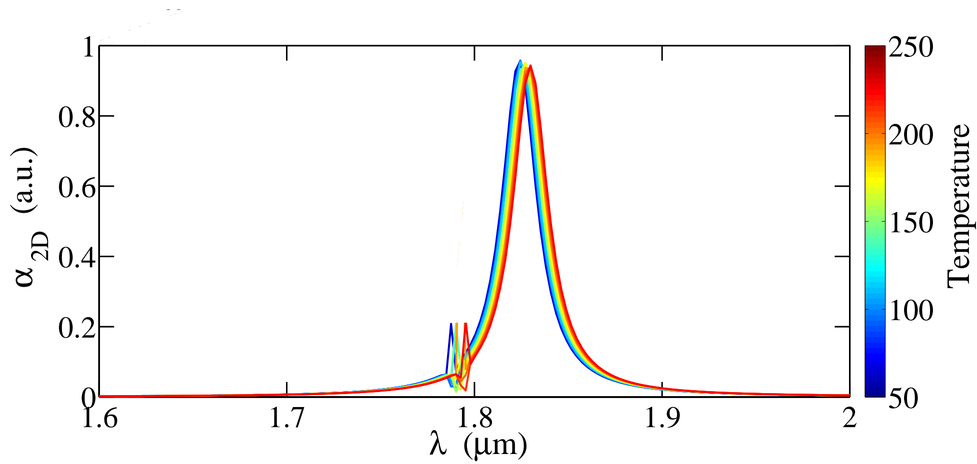

Figure 4.11: Absorption coefficient of GaN/AlGaN QCD operating at 1.85 μm.

The responsivity of the device is also presented and it follows the similar trend as found before. The responsivity decreases with increase of temperature as the scattering of carriers increases and relaxing carrier through designed path decreases. Hence, the escape probability (p_e) and quantum efficiency decreases, so does the overall performance of the device. The responsivity is shown in Fig. 4.12 where temperature is varied from 50 K to 250 K.

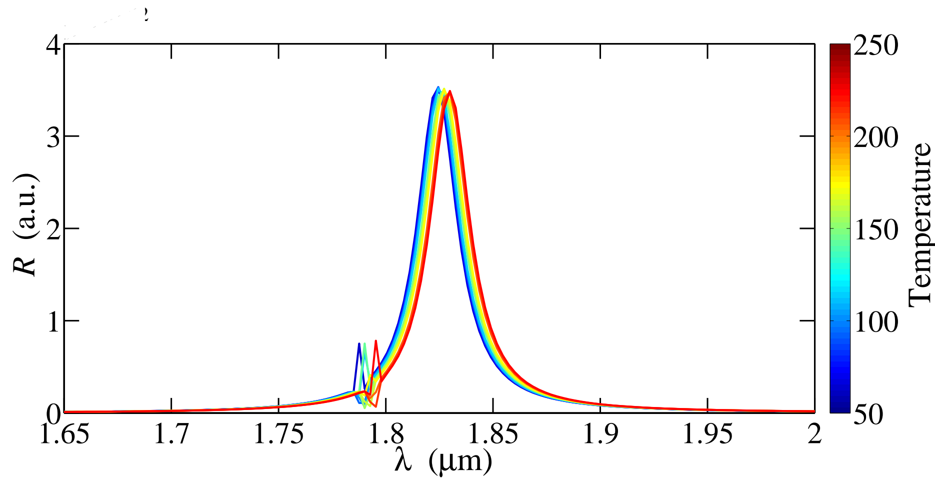

Figure 4.12: Responsivity of GaN/AlGaN QCD operating at 1.85 μm.

4.3 Proposed Mid-Infrared GaN/AlN QCD

GaAs-based QCLs have limitations of thermal backfilling and thermally activated phonon scattering which make it impossible for operation of the device at room temperature. These drawbacks can be overcome using III-N material systems, thanks to the large LO-phonon energy of 92 meV of GaN, which significantly exceeds the room-temperature thermal energy. Again, The higher bandgap offset of nitride material broadens the scoop to design in the shorter wavelength region. We have already presented a complete study of nitride based QCD operating at 1.85 μm [4]. But nitride QCD operating in the mid-infrared region remained unexplored till date. The mid-infrared spectral region of 2 – 20 μm contains strong characteristic vibrational transitions of many important molecules as well as two atmospheric transmission windows of 3 – 6μm and 8 – 13 μm, which makes it crucial for applications in spectroscopy, materials processing, chemical

and biomolecular sensing, security and industry [50]. In this work, we proposed two design for nitride QCDs both operating in the mid-infrared region (6.4 μm and 4.5 μm). The design was done by solving band structure using nitride material library of “QCL Simulation Package”. We also carried out the performance analysis using the developed simulator for nitride based mateial system.

4.3.1 Nitride QCD Design-1

4.3.1.1 Device Structure

A nitride based QCD is designed to detect in the mid-infrared region. GaN is used as the well material and $Al_{0.3}Ga_{0.7}N$ as the barrier material. It is designed to emit light in the 6.4 μm range. The conduction band diagram of one stage is shown schematically in Fig. 4.13 with the computed relevant wavefunctions. The layer widths of the structure are 40/ **20**/ 15/ **22**/ 19/ **25**/ 26/ **23**, where the layer sequences are given in Å, AlGaN barriers are in bold face, and GaN wells are in normal face. The proposed design of the detector consists of 40 periods.

The active region is n-type doped, so that there are available carriers to absorb light. When the light falls on the detector, carriers absorb light and get excited from the lower level, as shown in Fig. 4.13, to the upper level (blue bold line). Then excited carriers relax through the LO-phonon energy ladder to the ground state of the next stage.

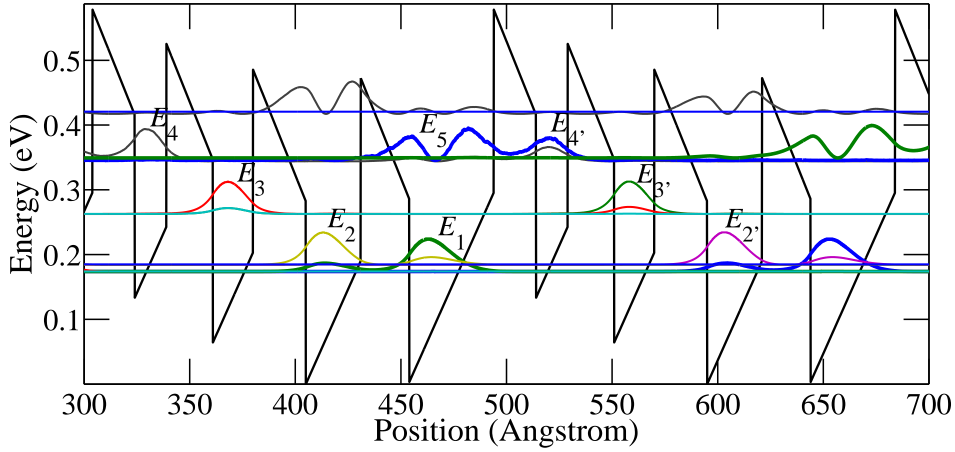

Figure 4.13: Band structure and the relevant moduli squared wavefunctions for active/relaxation region of design-1 at 200 K temperature. The layer sequence of a period of the structure, is <u>40</u>/ **20**/ 15/ **22**/ 19/ **25**/ 26/ **23**, where the layer sequences are given in Å, $Al_{0.3}Ga_{0.7}N$ barriers are in bold face, GaN wells are in normal face, and numbers underlined correspond to the n-doped layers (5×10^{17} cm^{-3}).

4.3.1.2 Transport Mechanism of the Device

The designed QCD given in Fig. 4.13 will absorb light around 6.35 μm (195 meV). When light having wavelength around 6.35 μm incident on the QCD, electrons of the ground state 1 can absorb the incident photon and be excited into one of the two upper states 5. From the excited states, the electrons have two extraction paths,

First, the excited electrons can scatter jump back to the ground state, which produces neither a net charge displacement nor any photocurrent. Second, the excited carriers can relax to the ground state of the next stage by emitting multiple LO-phonon. This second process leads to a displacement of these electrons along the growth direction (lateral in Fig. 4.13), which can finally be measured as current flowing between the two terminals of the

detector. A schematic representation of the energy levels is presented in Fig. 4.14. The arrow shows the transport path of the carrier in a QCD. The carriers in the energy level labeled as 1 absorbs light and excited to the enrgy level 5. Then the excited carries relax to the ground state of the next period through the relaxation path 5→4′→3′→2′ by emitting LO-phonon. As all states of the extraction cascade are arranged with an energy difference of ~92 meV, which is the energy of LO-phonon in GaN, the total extraction is fast and results in a high escape probability p_e.

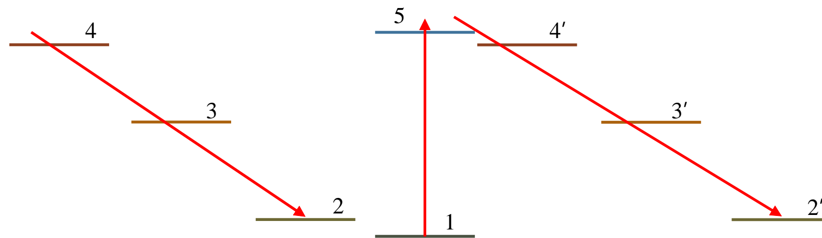

Figure 4.14: Schematic representation of QCD energy levels.

The model distinguishes between two classes of transitions: those taking place between states inside the same period (cascade) and those connecting states of adjacent periods of a repeated quantum cascade structure. The assumption that the former (intracascade transitions) are much stronger than the latter (intercascade transitions) then allows for the following description. Each period is considered to stay at thermodynamical equilibrium internally, but not necessarily to share the chemical potential with adjacent periods. Introducing a bias voltage between two periods as a perturbation and expressing the current due to that voltage leads to the main result of

that model, zero bias resistance (R_0A).

In the table 4.1, the intracascade rates have been shown for QCD design-1 structure. The transition rates in the relaxation path are faster compared to other scattering rates.

Table 4.1: Values of some transition rates in Nitride QCD design-1

Intersubband transition rate, G_{ij} ($s^{-1}m^{-2}$)	
G_{1-5}	1.15×10^{19}
G_{2-1}	2.7×10^{23}
G_{3-2}	2.05×10^{23}
G_{3-1}	1.84×10^{23}
G_{4-3}	1.10×10^{21}
G_{4-2}	1.39×10^{20}
G_{4-1}	2.55×10^{20}
$G_{5-4'}$	1.13×10^{18}

The rate equations for the energy levels in a period are solved to get the steady state carrier density of the structure. The LO-phono scattering rates are calculated, where the effect of light was incorporated through the incorporation of optical transition rates. The steady state carrier densities for T = 77 K and T = 200 K are shown in Fig. 4.15.

4.3.1.3 Zero Bias Resistance

Zero bias resistance, $R_0(T)A$ with A being the detector's surface area is a figure of merit for QCDs and other photovoltaic detectors, as they are

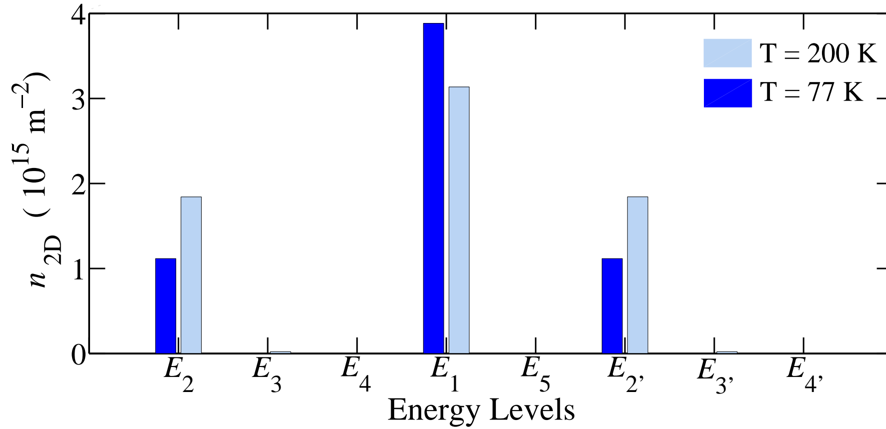

Figure 4.15: Carrier Density variation over temperature for designed GaN/AlN QCD design-1.

Johnson-noise limited above T_{BLIP}. Plotting the differential device resistivity logarithmically as a function of inverse device temperature, as shown in Fig. 4.16, is equivalent to usual Arrhenius plots. Evidently it is not possible to find exactly one activation energy from these data. At first glance, this is rather unsatisfactory, as I expected to find an activation energy which corresponds to the optical transition energy. But on a closer look, it becomes clear that a "two state" model is way too simple to explain electrical transport, as there is a series of states at energies situated between the lower and upper states of the optical transition which also contribute to electrical transport.

4.3.1.4 Current Density

The transport of carrier through the periods produces photocurrent and that can be calculated using the described model in Chap 3. The global current density of this device is shown in Fig. 4.16. The current density is compared with the device resistance (R_0A) in the figure.

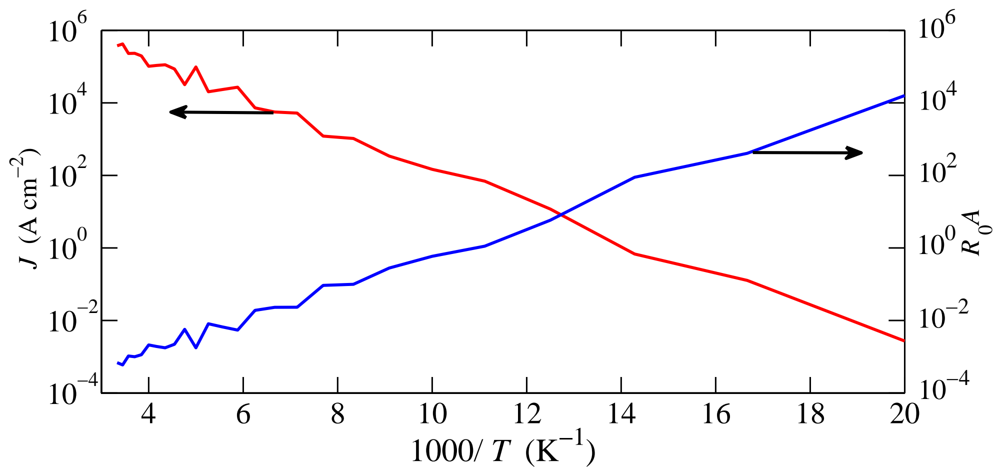

Figure 4.16: Current Density variation over temperature for designed GaN/AlN QCD design-1.

4.3.1.5 Absorption Coefficient Variation over Temperature

To calculate the absorption profile of the detector, a light consisting of wavelength ranging from 1 μm to 20 μm is used. The absorption peak is found at 6.4 μm at T = 150 K. The linewidth of the absorption spectrum was calculated using the interface roughness of the layers and it was found that the linewidth was about 27% of the transition energy.

The absorption coefficient is calculated for different temperature ranging from 50 K to 300 K and the results are given in Fig. 4.17. It is found that the absorption decreases with increasing temperature as is expected for other photovoltaic detectors. The peak absorption wavelength also shifts slightly due to variation of temperature. The shift in wavelength is about 0.05 μm for temperature variation from 40 K to 200 K.

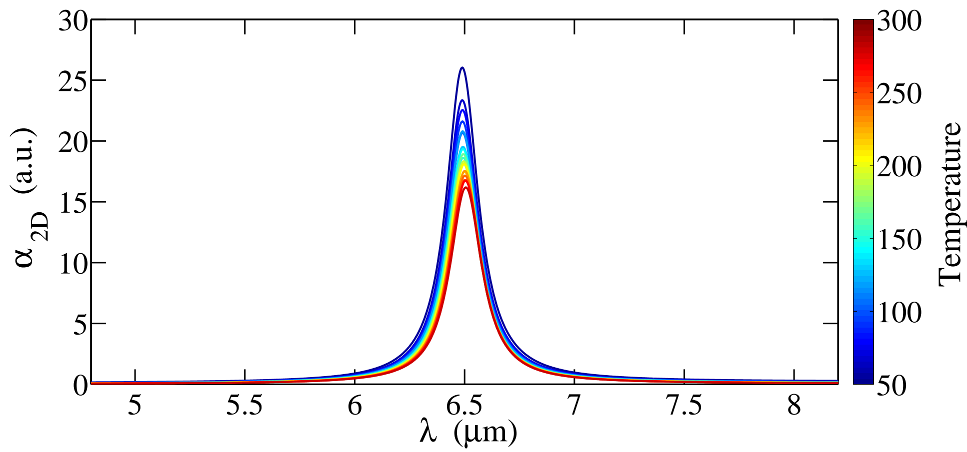

Figure 4.17: Absorption coefficient variation over temperature for designed GaN/AlN QCD design-1.

The decrease of absorption can be explained using the carrier distribution of the device. With the increase of temperature, the carrier from lower energy state (1) scatters to higher energy states. Due to the scattering of the carriers, the carrier density in the lower energy state N_i decreases and densities in the higher energy states increases. As a result, the difference of carrier density $N_i - N_j$ term in Eq. (3.23) decreases. So the absorption coefficient decreases which is shown in Fig. 4.17.

4.3.1.6 Quantum Efficiency

The overall quantum efficiency is calculated using the model described in section 3.4.3. The escape probability of the device is calculated using Eq. (3.25) and Eq. (3.26). It can be seen from Fig. 4.18 that with increase of temperature, the escape probability of the device drops and hence the quantum efficiency is also decreased.

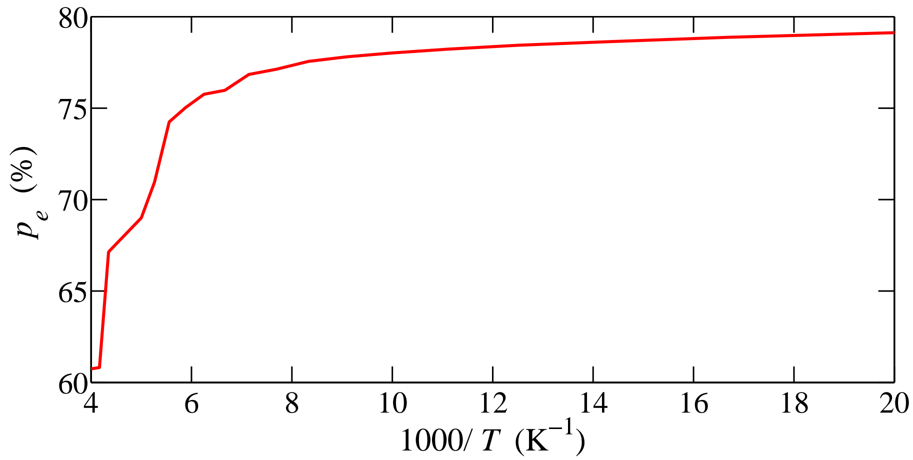

Figure 4.18: Escape probability variation over temperature for designed GaN/AlN QCD design-1.

At T = 150 K, we get the value of absorption efficiency achieved from Fig. 4.17 is η_{abs} = 18% and escape probability from Fig. 4.18 is p_e = 0.75. Using these values, we get the maximum achievable quantum efficiency from Eq. (3.24) is η_{tot} = 0.3375% for wavelength 6.4μm and number of periods N = 40. The quantum efficiency for this detector is higher than

reported GaAs QCD which is 0.038% for wavelength 5.3 μm [3]. We note that upto 150 K temperature p_e remains almost constant and above this temperature the values drop rapidly.

4.3.1.7 Responsivity Variation over Temperature

The responsivity of the detector is shown in Fig. 4.19 over the temperature range 50 K to 300 K. This shows a good match with the absorption spectrum and design transition energy. The calculated quantum efficiency is used to calculate the responsivity of the detector.

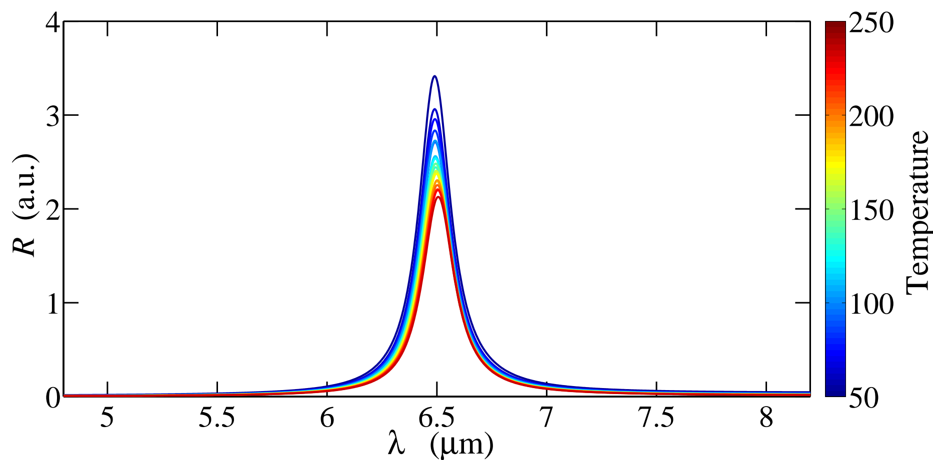

Figure 4.19: Responsivity variation over temperature for designed GaN/AlN QCD design-1.

The peak responsivity falls with increasing temperature and overall performance of the detector degrades. The main reason this degradation is the increase of carrier scattering and decrease of quantum efficiency. The change of peak responsivity is shown in Fig. 4.20. It can be seen from the

figure that peak responsivity falls about 2 times for temperature variation over 50 K to 300 K.

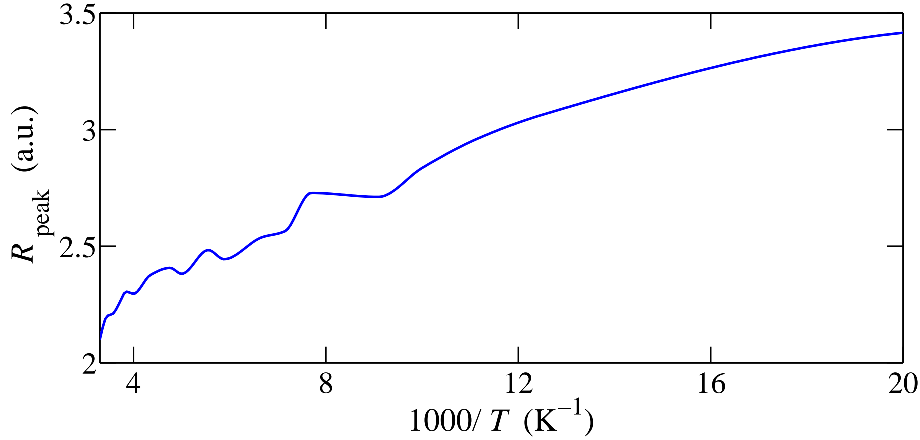

Figure 4.20: Peak Responsivity variation over temperature for designed GaN/AlN QCD design-1.

4.3.2 Nitride QCD Design-2

4.3.2.1 Device Structure

We propose another design of mid-infrared nitride based QCD. The design operating wavelength of this design is 4.5 μm. Again, the well material is wurtzite GaN and barrier material is $Al_{0.3}Ga_{0.7}N$. The design consists of 40 periods and each period consists of GaN well and $Al_{0.3}Ga_{0.7}N$ barrier superlattice structure. The layer widths of the structure are 30/ **23**/ 14/ **23**/ 18/ **28**/ 28/ **26**, where the layer sequences are given in Å, AlGaN barriers are in bold face, and GaN wells are in normal face. The first well is n-doped with doping concentration of 5×10^{11} cm^{-2}. The band structure of the

design is shown in Fig. 4.21.

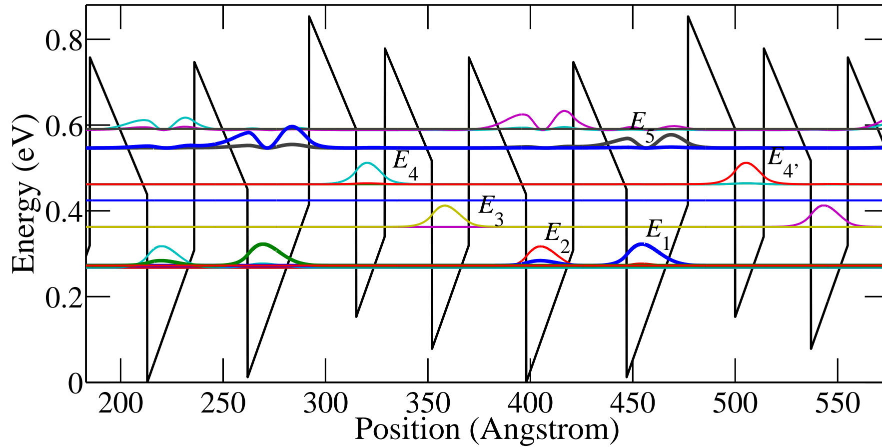

Figure 4.21: Band structure and the relevant moduli squared wavefunctions for active/relaxation region of design-2 at 200 K temperature. The layer sequence of a period of the structure, is <u>30</u>/ **23**/ 14/ **23**/ 18/ **28**/ 28/ **26**, where the layer sequences are given in Å, $Al_{0.3}Ga_{0.7}N$ barriers are in bold face, GaN wells are in normal face, and numbers underlined correspond to the n-doped layers (5×10^{17} cm^{-3}).

The transport of carrier is similar to the mechanism described in section 4.3.1.2. The lower and upper absorbing levels are shown in bold lines in Fig. 4.21. The relaxation path consists of LO-phonon energy ladder, which is 92 meV for GaN, is designed for fast transport and collection of carrier in the next period.

4.3.2.2 Transport Mechanism of the Device

The transport mechanism for nitride QCD is already defined earlier in this chapter. This design can also be explained using the same transport mechanism. In the Table 4.2, the intracascade rates have been shown for

QCD design-2 structure. The transition rates in the relaxation path is larger compared to other scattering rates.

Table 4.2: Values of some transition rates in Nitride QCD design-2

Intersubband transition rate, G_{ij} ($\mathbf{s^{-1}m^{-2}}$)	
G_{1-5}	2.9812×10^{20}
G_{2-1}	7.7×10^{20}
G_{3-2}	2.86×10^{20}
G_{3-1}	6.39×10^{15}
G_{4-3}	1.793×10^{20}
G_{4-2}	2.5696×10^{17}
G_{4-1}	4.8893×10^{11}
$G_{5-4'}$	7.131×10^{20}

The steady state carrier density for nitride QCD design-2 is shown in Fig. 4.22. The carriers are more scattered among the states for higher temperature for higher scattering rates as expected.

4.3.2.3 Zero Bias Resistance

The zero bias resistance (R_0A) is also calculated for this design. It is found that the resistance drops exponentially with increasing temperature as it is noted from nitride QCD design-1. The change in R_0A over temperature is presented in Fig. 4.23.

If we take a closer look at the R_0A for different structure of nitride based QCD, then it can be concluded that R_0A for a specific temperature increases with the decrease of operating wavelength of the design. It can be easily

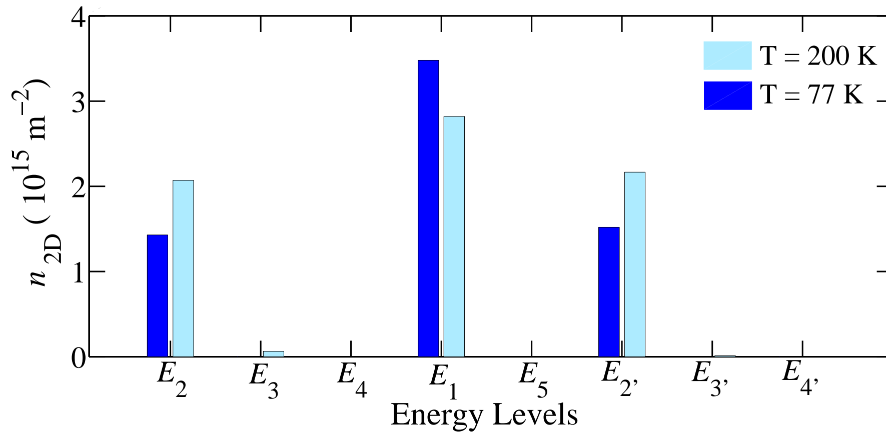

Figure 4.22: Carrier Density variation over temperature for designed GaN/AlN QCD design-2.

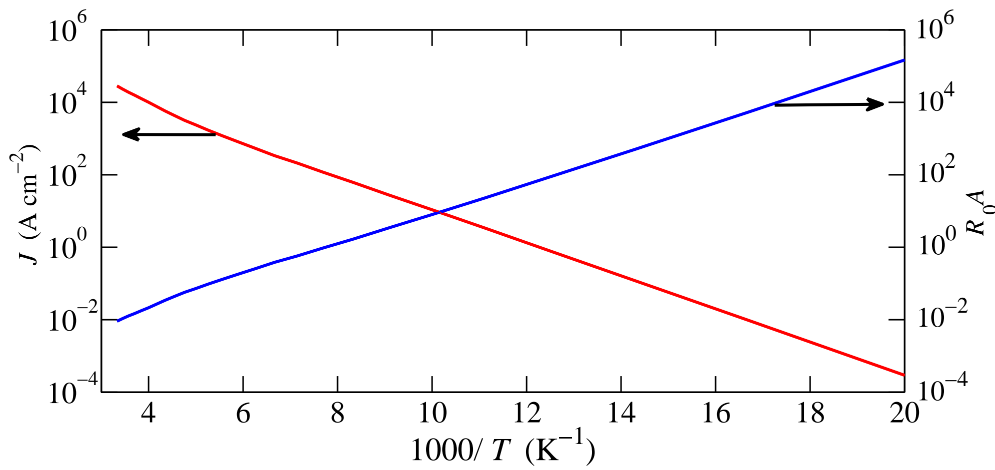

Figure 4.23: Zero bias resistance and current density for designed GaN/AlN QCD design-2 for T = 50 K to T = 300 K.

explained with the transition energy value. With higher separation of energy levels may essentially result into higher resistance of the device. This change can be shown in Fig. 4.24. It was found that the proposed nitride based QCDs have higher resistance than InGaAs/InAlAs QCD designed to operated at 5.2 μm. The zero bias resistance of GaAs/AlGaAs was also found comparable with the proposed nitride based QCDs.

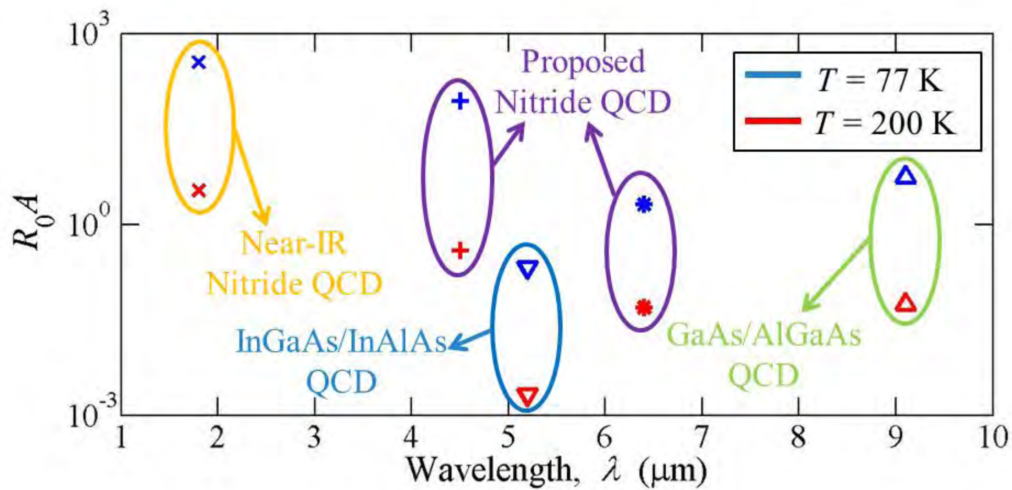

Figure 4.24: Zero bias resistance variation for different nitride based QCD for T = 77 K and T = 200 K.

4.3.2.4 Current Density

The current density, J is inversely related to the zero bias resistance of the device. The current density increases with the decrease of resistance of the device which is shown in Fig. 4.23.

4.3.2.5 Absorption Coefficient Variation over Temperature

The absorption coefficient of nitride based QCD design-2 was calculated for different temperature ranging from 50 K to 300 K and the trend of changing absorption coefficient was found same as it was seen before. The peak absorption decreases with temperature rise. The peak absorption wavelength also shifts slightly due to variation of temperature. The shift in wavelength is about 0.01 μm for temperature variation from 50 K to 200 K. The result is shown in Fig. 4.25.

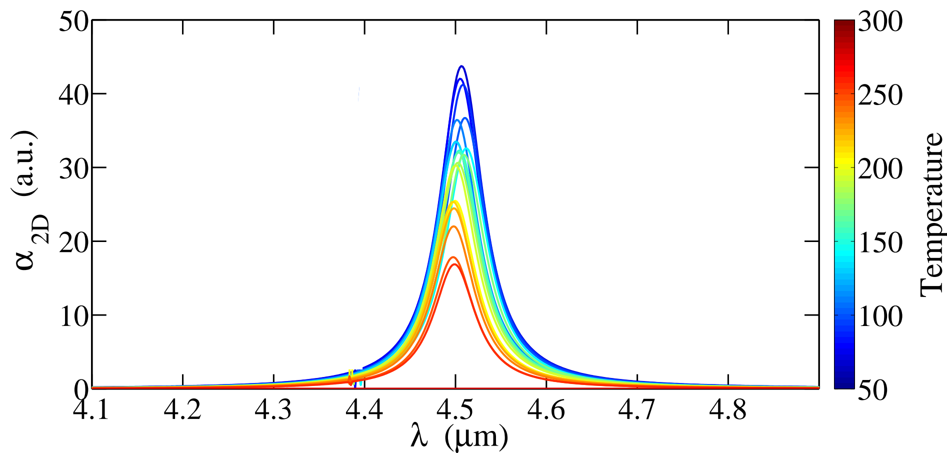

Figure 4.25: Absorption coefficient variation over temperature for designed GaN/AlN QCD design-2.

4.3.2.6 Quantum Efficiency

The overall quantum efficiency is again calculated using the model described in section 3.4.3. It can be seen from Fig. 4.26 that with increase of temperature, the escape probability of the device drops and hence the

quantum efficiency is also decreased.

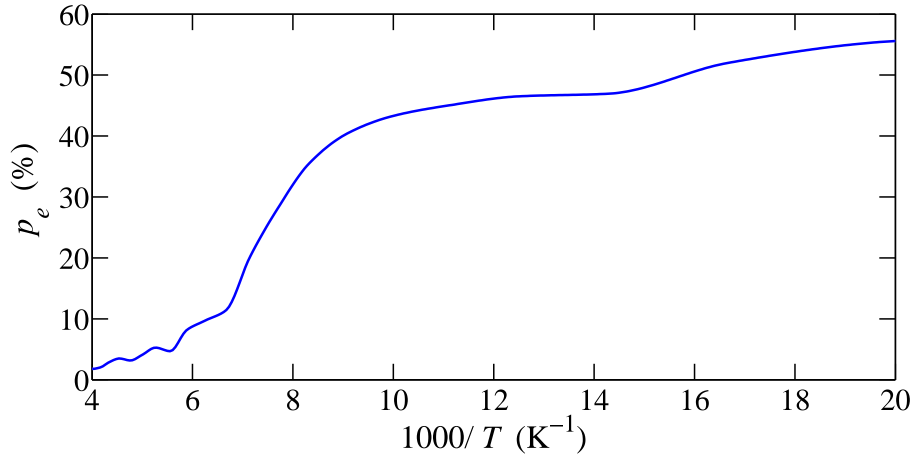

Figure 4.26: Escape probability variation over temperature for designed GaN/AlN QCD design-2.

At T = 150 K, we get the value of absorption efficiency achieved from Fig. 4.25 is η_{abs} = 30% and escape probability from Fig. 4.26 is p_e = 0.35. Using these values, we get the maximum achievable quantum efficiency from Eq. (3.24) is η_{tot} = 0.4375% for wavelength 6.4μm and number of periods N = 40.

4.3.2.7 Responsivity Variation over Temperature

The responsivity of this design was also calculated for the temperature range of 50 K to 250 K and shown in Fig. 4.27. The peak responsivity is also found to be decreasing in this design. The decrease of magnitude is slower in the lower temperature range, but it changes very rapidly after

T = 200 K. The responsivity almost drops to zero at T = 250 K. The change of peak responsivity is presented in Fig. 4.28.

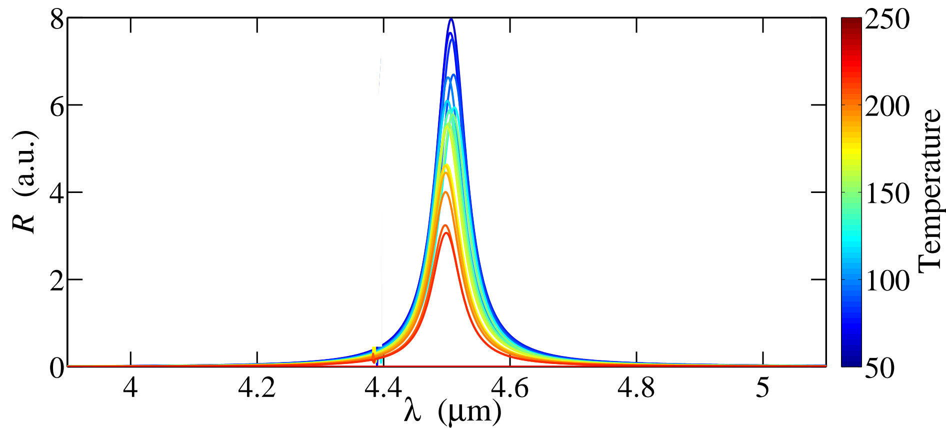

Figure 4.27: Responsivity variation over temperature for designed GaN/AlN QCD design-2.

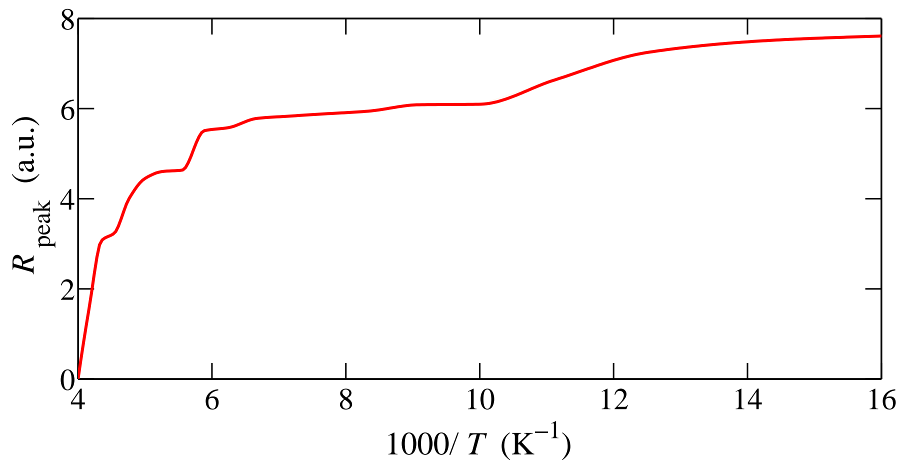

Figure 4.28: Peak Responsivity variation over temperature for designed GaN/AlN QCD design-2.

4.4 Summary

The summary of this chapter is presented below,

- We presented the verification of the developed model in the beginning of the chapter. Three separate designs for QCD are studied and results were very close to the reported values, that verifies our developed simulator.
- We explained the transport mechanism in a QCD and a model is presented using the tranposrt of carrier in the structure to calculated zero bias resistance of the device.
- We presented the performance analysis of the nitride based mid-infrared QCDs over the variation of temperature through different performance parameters like R_0A, quantum efficiency, and Responsivity.
- We described the absorption in a single period of the QCD and studied the effect of temperature effect on the performance of the device.
- Finally, we presented two designs of nitride based mid-infrared QCD having operating wavelengths of 6.4 μm and 4.5 μm with optimized design and doping in the active region.
- The maximum achievable quantum efficiency of the QCD designed in this work is 0.34% and 0.44% for the operating wavelength of 6.4 μm and 4.5 μm respectively.

- Nitride based QCD designed to operate at 6.4 μm shows comparatively higher temperature operation (~150 K) than GaAs/AlGaAs QCD designed to operate at 5.3 μm reported in [44].

Chapter 5

Conclusion

The aim of this work was directed to understanding of the material issues involved in the GaN/AlGaN ISB technology, mainly targeting mid-IR operation, and to try to achieve operation of nitride based heterostructures at even longer wavelength. The accomplishments in these fields are described below.

In the first part of this work, a material library for the nitride material is developed to simulate the nitride based structures. The solution of the band structure was done by solving Schrodinger equation using finite difference matrix (FDM) method. The material library was developed to provide material system information needed in FDM method. The polarization effect of the nitride material leads to development of internal electric field, which plays a vital role in the solution of band structure. The strain effect and internal electric field effect was incorporated to get a more accurate simulator of nitride based structures. The simulator was verified by comparing

results with different experimental reports and in almost all the cases, the results fairly matched.

In this work, a nitride based mid-infrared detector has been developed. Thanks to its photovoltaic operation scheme, it eliminates in a most efficient way one of the dominating noise sources of QWIPs, namely dark current noise. In order to operate such a detector, an internal potential gradient rather than an external voltage bias is responsible for the vertical transport of the electrons. In the case of quantum cascade detectors, as explored in this work, this internal potential gradient is provided by a carefully designed series of quantum wells with increasing width. The latter provides an efficient electron extraction cascade towards the ground state of the following active region period.

Most of the photovoltaic detectors have very low detectivity at higher temperature. The scattering of carriers at higher temperature affects the performance of the detectors. Nitride material system was a very good choice for detector design as it shows higher resistance due to its inherent internal electric field. The performance of the designed structures were studied for temperature variation. The performance parameters that were evaluated were zero bias resistance, absorption coefficient, quantum efficiency, and responsivity. The resistance of the device was found higher in this nitride based QCD designs. The variation of resistance with temperature showed that with temperature resistance get lowered and as a result noise current density increases drastically. That limits the performance of

the detectors in the higher temperature.

The important performance parameter, quantum efficiency of the structure was studied in this work. The escape probability of the carrier was calculated using the scattering rates. The quantum efficiency (QE) of the nitride based QCDs were found comparatively higher in the higher temperature. The calculated values of QE are 0.34% and 0.44% respectively for 6.4 μm and 4.5 μm operating wavelength detectors. The responsivity of the detectors were also studied and presented in this work.

Overall, a detail study of nitride material system is presented and two optimized designs of nitride based mid-infrared QCD are proposed in this work. Apart from the design proposition, the complete study of the performance analysis with the variation of temperature is given. It can be argued that nitride based mid-IR QCDs can be the next generation of sensors for its better performance in the mid-IR region in terms of noise and quantum efficiency and possibility of monolithic fabrication process with QCL.

Bibliography

[1] Y. Kotsar, “Puits quantiques GaN/Al (Ga) N pour l’optolectronique inter-sous-bande dans l’infrarouge proche, moyen et lointain,” Ph.D. dissertation, Institute for Nanoscience and Cryogenics at CEA-Grenoble, France, 2012.

[2] C. Koeniguer, L. Gendron, X. Marcadet, and V. Berger, “Characterization and Modeling of a Quantum Cascade Detector,” *Proc. of SPIE*, vol. 5783, pp. 767–776, 2005.

[3] M. Gaft, “Design and characterisation of far- and mid-infrared quantum cascade detectors,” Ph.D. dissertation, Institut de Physique, Universite de Nauchatel, 2006.

[4] A. Vardi, G. Bahir, F. Guillot, C. Bougerol, and E. Monroy, “Near infrared quantum cascade detector in GaN/AlGaN/AlN heterostructures,” *Applied Physics Letters*, vol. 92, p. 011112, 2008.

[5] L. C. West and S. J. Eglash, “First Observation of an extremely large-dipole infrared transition within the conduction band of a GaAs quantum well,” *Applied Physics Letters*, vol. 46(12), pp. 1156–1158, 1985.

[6] J. Faist, F. Capasso, D. L. Sivco, C. Sirtori, A. L. Hutchinson, and A. Y. Cho, "Quantum Cascade Laser," *Science*, vol. 264, pp. 553–556, 1994.

[7] B. F. Levine, R. J. Malik, J. Walker, K. K. Choi, C. G. Bethea, D. A. Kleinman, and J. M. Vandenberg, "Strong 8.2 μm infrared intersubband absorption in doped GaAs/AlAs quantum well waveguides," *Applied Physics Letters*, vol. 50(5), pp. 273–275, 1987.

[8] A. Harwit and J. J. S. Harris, "Observation of Stark shifts in quantum well intersubband transitions," *Applied Physics Letters*, vol. 50(11), pp. 685–687, 1987.

[9] B. F. Levine, K. K. Choi, C. G. Bethea, J. Walker, and R. J. M. Malik, "New 10 μm infrared detector using intersubband absorption in resonant tunneling GaAlAs superlattices," *Applied Physics Letters*, vol. 50, p. 1092, 1987.

[10] B. F. Levine, "Quantum-well infrared photodetectors," *Journal of Applied Physics*, vol. 74(8), pp. R1–R81, 1993.

[11] H. C. Liu, *Semiconductors and semimetals*. Academic Press, San Diego, 2000, vol. 62, no. Chapter 3.

[12] H. Schneider, "Optimized performance of quantum well intersubband infrared detectors: Photovoltaic versus photoconductive operation," *Journal of Applied Physics*, vol. 74(7), pp. 4789–4791, 1993.

[13] C. Schnbein, H. Schneider, G. Bihlmann, K. Schwarz, and P. Koidl,

"A 10 μm GaAs/$Al_xGa_{1-x}As$ intersubband photodetector operating at zero bias voltage," *Applied Physics Letters*, vol. 68, pp. 973–975, 1996.

[14] H. Schneider, C. Schnbein, G. Bihlmann, P. van Son, and H. Sigg, "High-speed infrared detection by uncooled photovoltaic quantum well infrared photodetectors," *Applied Physics Letters*, vol. 70, pp. 1602–1604, 1997.

[15] G. Hasnain, B. F. Levine, D. L. Sivco, and A. Y. Cho, "Mid-infrared detectors in the 3-5 μm band using bound to continuum state absorption in InGaAs/InAlAs multiquantum well structures," *Applied Physics Letters*, vol. 56(8), pp. 770–772, 1990.

[16] G. Sarusi, S. D. Gunapala, J. S. Park, and B. F. Levine, "Design and performance of very long-wavelength GaAs/$Al_xGa_{1-x}As$ quantum-well infrared photodetectors," *Journal of Applied Physics*, vol. 76(10), pp. 6001–6008, 1994.

[17] L. Gendron, M. Carras, A. Huynh, V. Ortiz, C. Koeniguer, and V. Berger, "Quantum cascade photodetector," *Applied Physics Letters*, vol. 85, p. 2824, 2004.

[18] V. Berger, French Patent no. 0 109 754, 2001.

[19] J. Wu, "When group-III nitrides go infrared: New properties and perspectives," *Journal of Applied Physics*, vol. 106, p. 011101, 2009.

[20] J. R. Lang, C. J. Neufeld, C. A. Hurni, S. C. Cruz, E. Matioli, U. K. Mishra, and J. S. Speck, "High external quantum efficiency and fill-

factor InGaN/GaN heterojunction solar cells grown by NH_3-based molecular beam epitaxy," *Applied Physics Letters*, vol. 98, p. 131115, 2011.

[21] V. Y. Davydov, A. Klochikhin, V. Emtsev, D. Kurdyukov, S. Ivanov, V. Vekshin, F. Bechstedt, J. Furthmller, J. Aderhold, J. Graul, A. Mudryi, H. Harima, A. Hashimoto, A. Yamamoto, and E. Haller, "Band Gap of Hexagonal InN and InGaN Alloys," *Physica Status Solidi B*, vol. 34, p. 787 795, 2002.

[22] B. S. Ma, W. J. Fan, Y. X. Dang, W. K. Cheah, W. K. Loke, W. Liu, D. S. Li, S. F. Yoon, D. H. Zhang, H. Wang, and C. H. Tung, "GaInNAs double-barrier quantum well infrared photodetector with the photodetection at 1.24 μm," *Applied Physics Letters*, vol. 91, p. 051102, 2007.

[23] S. D. Gunapala, S. V. Bandara, J. K. Liu, C. J. Hill, S. B. Rafol, J. M.Mumolo, J. T. Trinh, M. Z. Tidrow, and P. D. LeVan, "Development of midwavelength and long-wavelength megapixel portable QWIP imaging cameras," *Infrared Phys. Technol.*, vol. 47, p. 67 75, 2005.

[24] C. Walther, M. Fischer, G. Scalari, R. Terazzi, N. Hoyler, and J. Faist, "Quantum cascade lasers operating from 1.2 to 1.6 THz," *Applied Physics Letters*, vol. 91, p. 131122, 2007.

[25] Q. K. Yang, C. Manz, W. Bronner, K. Kohler, and J. Wagner, "Room-temperature short-wavelength (λ 3.73.9 μm) GaInAs/AlAsSb quantum-cascade lasers," *Applied Physics Letters*, vol. 88, p. 121127, 2006.

[26] F. R. Giorgetta, E. Baumann, M. Graf, L. Ajili, N. Hoyler, M. Giovannini, J. Faist, D. Hofstetter, P. Krtz, and G. Sonnabend, “16.5 μm quantum cascade detector using miniband transport,” *Applied Physics Letters*, vol. 90, p. 231111, 2007.

[27] S. Adachi, “GaAs and Related Materials: Bulk Semiconducting and Superlattice Properties,” World Scientific Publishing Company, Tech. Rep., 1994.

[28] G. Scalari, C. Walther, M. Fisher, R. Terazzi, H. Beere, D. Ritchie, and J. Faist, “THz and sub-THz quantum cascade lasers,” *Laser and Photon.*, vol. 3, p. 45, 2009.

[29] S. Kumar, Q. Hu, and J. L. Reno, “186 K operation of terahertz quantum-cascade lasers based on a diagonal design,” *Applied Physics Letters*, vol. 94, p. 131105, 2009.

[30] B. S. Williams, S. Kumar, Q. Hu, and J. L. Reno, “Magnetotunneling spectroscopy of resonant anticrossing in terahertz intersubband emitters,” *Applied Physics Letters*, vol. 79, p. 4444, 2001.

[31] N. Iizuka, K. Kaneko, N. Suzuki, T. Asano, S. Noda, and O. Wada, “Ultrafast intersubband relaxation (150 fs) in AlGaN/GaN multiple quantum wells,” *Applied Physics Letters*, vol. 77, p. 648, 2000.

[32] P. Rinke, M. Scheffler, Qteish, M. Winkelnkemper, D. Bimberg, and J. Neugebauer, “Band gap and band parameters of InN and GaN from quasiparticle energy calculations based on exact-exchange density-functional theory,” *Applied Physics Letters*, vol. 89, p. 161919, 2006.

[33] E. S. Hellman, "The polarity of GaN: a critical review," MRS Internet J. N. S. R. 3, 1-12, Tech. Rep., 1998.

[34] T. Fujii, Y. Gao, R. Sharma, E. L. Hu, S. P. DenBaars, and S. Nakamura, "Increase in the extraction efficiency of GaN-based light-emitting diodes via surface roughening," *Applied Physics Letters*, vol. 84, p. 855, 2004.

[35] I. Vurgaftman and J. R. Meyer, "Band parameters for nitrogen-containing semiconductors," *Journal of Applied Physics*, vol. 94, p. 3675, 2003.

[36] F. Bernardini and V. Fiorentini, "Macroscopic polarization and band offsets at nitride heterojunctions," *Physical Review B*, vol. 57(16), p. R9427, 1998.

[37] S. Elhamri, R. S. Newrock, D. B. Mast, M. Ahoujja, W. C. Mitchel, J. M. Redwing, M. A. Tischler, and J. S. Flynn, "$Al_{0.15}Ga_{0.85}N$/GaN heterostructures: Effective mass and scattering times," *Physical Review B*, vol. 57(3), p. 1374, 2002.

[38] E. Baumann, "Near infrared intersubband absorption and photovoltaic detection in GaN/AlN multi quantum well structures," Ph.D. dissertation, University of Neuchatel, 2007.

[39] O. Ambacher, J. Majewski, C. Miskys, A. Link, M. Hermann, M. Eickhoff, M. Stutzmann, F. Bernardini, V. Fiorentini, V. Tilak, B. Schaff, and L. F. Eastman, "Pyroelectric properties of Al(In)GaN/GaN hetero- and

quantum well structures," *Journal of Phys.: Condens. Matter*, vol. 14, pp. 3399–3434, 2002.

[40] J. Piprek, *Nitride Semiconductor Devices- Principles and Simulation*. Wiley Publication, 2007.

[41] H. Zhao, R. A. Arif, Y.-K. Ee, and N. Tansu, "Self-Consistent Analysis of Strain-Compensated InGaN/AlGaN Quantum Wells for Lasers and Light-Emitting Diodes," *IEEE Journal of Quantum Electronics*, vol. 45(1), 2009.

[42] M. Helm, *The Basic Physics of Intersubband Transitions*. Academic Press, San Diego, 2000.

[43] G. Bastard, "Wave mechanics apllied to semiconductor heterostructures," Monographies de physiques. Les editions de physique, Les Ulis, France, Tech. Rep., 1996.

[44] C. Koeniguer, G. Dubois, A. Gomez, and V. Berger, "Electronic Transport in Quantum Cascade Structures at Equilibrium," *Physical Review B*, vol. 74, p. 235325, 2006.

[45] R. Ferreira and G. Bastard, "Evaluation of some scattering times for electrons in unbiased and biased single- and multiple-quantum-well structures," *Physical Review B*, vol. 40, p. 1074, 1989.

[46] R. Paiella, *Intersubband Transitions in Quantum Structures*. McGraw-Hill, New York, 2006.

[47] e. a. Rostami, A., "Lecture Notes in Electrical Engineering," *Terahertz Technology*, vol. 77, 2011.

[48] A. Gomez, M. Carras, A. Nedelcu, E. Costard, X. Marcadet, and V. Berger, "Advantages of Quantum Cascade Detectors," *Proc. of SPIE*, vol. 6900, pp. 69 000J–1, 2008.

[49] L. Gendron, C. Koeniguer, X. Marcadet, and V. Berger, "Quantum Cascade Detection," *Proc. of SPIE*, vol. 5612, pp. 63–71, 2004.

[50] A. Schliesser, N. Picqu, and T. W. Hnsch, "Mid-infrared frequency combs," *Nature Photonics*, vol. 6(7), pp. 440–449, 2012.